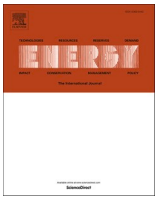
Energy 336 (2025) 138365



Contents lists available at ScienceDirect

Energy

journal homepage: www.elsevier.com/locate/energy





Transient cooling wall temperatures of supercritical carbon dioxide boiler during load variation process

Binghan Ma [a], Jinliang Xu [a,b,*], Haonan Zheng [a], Tianze Wang [a], Jian Xie [a,b]

[a] Beijing Key Laboratory of Multiphase Flow and Heat Transfer for Low Grade Energy Utilization, North China Electric Power University, Beijing, 100026, China
[b] Key Laboratory of Power Station Energy Transfer Conversion and System (North China Electric Power University), Ministry of Education, Beijing, 102206, China

ARTICLE INFO

Handling Editor: Dr L Luo

Keywords:
sCO_2 modular boiler
Load variation
Cooling wall temperature
Dynamic model
sCO_2 coal-fired power generation system

ABSTRACT

Efficient and flexible coal-fired supercritical carbon dioxide (sCO_2) power plant is helpful to balance unstable renewable energies, available studies focus on transient sCO_2 cycle analysis without coupling the sCO_2 boiler heat source. Here, we explore thermal-hydraulic characteristics of sCO_2 boiler during load variation process for a 300 MWe power plant. Modular boiler is applied to eliminate ultra-large pressure drop induced efficiency penalty, with analysis focused on two high heat flux modules of Part 1 and Part 2. The fluid-solid coupling model calculates spatiotemporal cooling wall temperatures by considering circumferential non-uniformity of furnace heat flux ($\eta_{q,c}$), using the accurate heat transfer coefficient correlation of sCO_2 in tubes developed by our group. We demonstrate that during both load increase (50 %THA to 100 %THA) and decrease (100 %THA to 50 %THA) with load variation rates (LVRs) ranging from ±2 % to ±10 %Pe/min, the hot spot temperatures of cooling wall remain below the material temperature limit of 705 °C. In Part 1, hot spot temperature increases with LVR during load increase process, reaching 685.8 °C at 10 %Pe/min under $\eta_{q,c} = 1.1$. In Part 2, hot spot temperature remains constant at 698.2 °C across all LVRs under the same condition. However, temperature change rates increase with |LVR|, maintaining below the 5 K/min limit when LVR is smaller than (6.2–6.3) % Pe/min. We conclude important effect of the load variation rate on the temperature change rate of cooling walls, which dominates thermal stress of cooling walls.

1. Introduction

Carbon dioxide is non-toxic, non-flammable, colorless and tasteless. Supercritical carbon dioxide (sCO_2) cycle recovers heat from heat source to generate CO_2 vapor for power generation. Compared with Rankine cycle with water-steam as the working fluid, sCO_2 cycle has benefits of higher efficiency, more compactness and flexibility [1]. To develop green energy technologies, many countries put great efforts in research and development of sCO_2 cycles, driven by nuclear energy, solar energy, waste heat, and fossil energy. Abundant studies have been conducted on the cycle analysis [2,3], development of components such as heat exchangers [4], compressors and turbines [5,6]. Recent progress on the development of sCO_2 power generation technologies is reviewed in Refs. [7–9].

Recently, dynamic characteristics of sCO_2 cycle have been paid attention. Jiang et al. [4] established a dynamic model of the Printed Circuit Heat Exchanger (PCHE), demonstrating the weight reduction by 30 % compared to conventional shell-and-tube heat exchangers. Moreover, the time constants for variations in inlet temperature and flow rate are less than 2 min. Regarding the system's response to disturbances, Ma et al. [10] observed that among various parameters, the sCO_2 cycle exhibited the fastest dynamic response to abrupt changes in the main gas temperature, compared to variations in pressure and mass flow rate. Furthermore, the recompression cycle accommodated a wider range of load variation than the simple regenerative cycle. Deng et al. [11] applied a sinusoidal signal to the heat-side inlet temperature of the PCHE and observed that key thermodynamic parameters including temperature, component power and cycle efficiency exhibit sinusoidal fluctuations with the same period. Regarding the system's start-up and shutdown behavior, Liese et al. [12] developed a dynamic model of a 10 MWe recompression cycle to simulate its start-up and shutdown processes. They achieved a load variation rate of 7.5 %/min using only storage control and sliding pressure operation. Wang et al. [13] conducted a comprehensive comparison and evaluation of storage control,

* Corresponding author. Beijing Key Laboratory of Multiphase Flow and Heat Transfer for Low Grade Energy Utilization, North China Electric Power University, Beijing, 100026, China.
E-mail address: xjl@ncepu.edu.cn (J. Xu).

https://doi.org/10.1016/j.energy.2025.138365
Received 24 April 2025; Received in revised form 14 August 2025; Accepted 4 September 2025
Available online 15 September 2025
0360-5442/© 2025 Elsevier Ltd. All rights are reserved, including those for text and data mining, AI training, and similar technologies.

valve control, and coupled control, assessing their performance in terms of safety, efficiency, and load variation range. Wang et al. [14] presented a detailed review of dynamic modeling, experimental setups, and control strategies for start-up, shutdown, and load following in the sCO_2 Brayton cycle system.

In China, the development of coal-fired sCO_2 power generation technology is useful to balance unstable renewable energies [15,16]. As a key component, sCO_2 boiler provides heat to drive the cycle [17]. Investigations have been conducted to address challenges when coupling the sCO_2 boiler with the cycle. Firstly, under the same capacity, the flow rate in the sCO_2 boiler is 6–8 times of that in a conventional water-steam boiler, leading to substantially greater pressure drops. If conventional boiler designs are adopted, it would increase the power demand of the compressor and consequently lower the cycle efficiency. To address this issue, Xu et al. [1] proposed a modular configuration for sCO_2 boiler. In this scheme, both the length of each module and the corresponding mass flow rate are halved, reducing the pressure drop significantly. Secondly, the moderate and low temperature flue gases are underutilized due to higher CO_2 temperatures entering the boiler. To overcome this limitation, Sun et al. [3] proposed a novel combined cycle, in which the top cycle, bottom cycle and air preheater absorb heat from high, moderate and low temperature flue gases, respectively. Furthermore, they introduced overlap energy utilization principle to balance the efficiencies of the top and bottom cycles. This allowed for the integration of components from both cycles, thereby reducing the total number of system components [2].

Due to higher CO_2 temperatures entering the cooling walls, and limited heat transfer coefficients of CO_2 in tubes [18], maintaining cooling wall temperatures at a desired level is a challenging issue. Based on thermal coupling between radiation heat flux in furnace side and CO_2 fluid in cooling wall tubes, Ref. [19] proposed a comprehensive solution to decrease cooling wall temperatures, including four techniques: (i) improved coupling in furnace width direction (CWD), (ii) flue gas recirculation for heat flux reduction (FGR), (iii) improved coupling in furnace height direction (CHD), and (iv) enhanced heat transfer in cooling wall tubes (EHT). A comprehensive thermal hydraulic model is developed for a 1000 MWe power plant. It is found that these solutions reduce cooling wall temperatures from 670.5 °C to 635.0 °C, among which CWD, FGR, CHD and EHT contribute to the decrement of cooling wall temperatures by 13.3 °C, 4.4 °C, 6.8 °C and 11.0 °C, respectively.

It is noted that sCO_2 boiler possesses significant thermal inertia due to combustion in furnace and convective heat transfer in tubes, creating slow response to load variations. The thermal inertia is a key factor limiting the unit's load variation rate (LVR) and load regulation range. To enhance the unit's operational flexibility, it is essential not only to improve the boiler's response to load variation and increase its load regulation range, but also to ensure the safe operation of the boiler during peak shaving. For supercritical-water boiler, abundant researches have been conducted on the dynamic characteristics of the cooling wall [20–22]. However, these results may not be extended to the sCO_2 boiler due to significantly different physical properties of water/-steam and CO_2, and different configurations of the two boilers. Investigations on the transient cooling wall temperatures of sCO_2 boiler are very limited. Liu et al. [23] performed comparative studies of supercritical coal-fired boilers using water-steam and CO_2 as the working fluids, respectively. A novel 600 MW sCO_2 boiler design was proposed, and its dynamic model was established and validated. They showed that when the CO_2 mass flow rate and coal feed rate are suddenly reduced by 5 %, the main CO_2 temperature changes by +5.5 °C and −6.1 °C, with response times of 220 s and 250 s, respectively. The sCO_2 boiler demonstrates a response time approximately 700 s shorter than that of the supercritical water boiler under identical disturbance conditions.

In summary, existing studies focus on transient sCO_2 cycle analysis without coupling the heat source of the sCO_2 boiler. Ensuring the safe operation of the sCO_2 boiler during load variation process is critical to achieving flexible operation of sCO_2 coal-fired power generation system. In this study, a 300 MW sCO_2 modular boiler is selected as the research subject. The temperature variations of the cooling wall are analyzed during both load increase and decrease processes at different LVRs. We aim to address the following questions: Does the hot spot temperature exceed the material limit during the load variation process? How does the location of the hot spot change? What is the temperature change rate of the cooling wall during load variation process? How do different LVRs affect the above issues? To answer the above questions, we developed a transient fluid-solid coupling model of the cooling wall of sCO_2 boiler. Non-uniform heat flux distribution in the furnace width direction is considered by introducing a circumferential non-uniformity factor. The CO_2 flow in the tube is described by a one-dimensional transient model, while a two-dimensional model for the tube wall accounts for radial and circumferential heat conduction. The dynamic thermal response of the cooling wall during load variation is systematically analyzed by simulating changes in inlet temperature, pressure, mass flow rate, and furnace heat flux. The findings of this study provide theoretical support for the safe operation and control strategy development of sCO_2 coal-fired power generation units during load variation process. The structure of this paper is organized as follows: Section 2 presents the sCO_2 cycle coupling with the boiler. Section 3 presents the unsteady fluid-solid coupling model of the cooling wall. Section 4 discusses the results. Conclusions are summarized in Section 5.

2. sCO_2 cycle coupling with boiler

The 300 MW sCO_2 coal-fired power generation system is illustrated in Fig. 1a. The system adopts the connected-top-bottom-cycle and the overlap energy utilization principle to maximize the use of boiler flue gas heat. This approach eliminates the efficiency gap between the top and bottom cycles [2]. The top cycle employs a once-reheat recompression cycle (RC + RH). The bottom cycle adopts a recompression reheating cycle with an external air preheater (RC + RH + EAP). The system operates as follows: After expansion in the low-pressure turbine (T2), the working fluid splits and enters the top and bottom cycles. The working fluid entering the top cycle passes through the high-temperature recuperator (HTR) and the low-temperature recuperator (LTR), and then splits. One part enters the auxiliary compressor (C2), while the other flows into the main compressor branch (C1), passes through the LTR, and then splits again. One part merges with the outlet fluid from the C2, enters the top cycle, absorbs heat, and reaches point 5. The other part enters the bottom cycle, absorbs heat, and reaches point 5b. The CO_2 from both the top and bottom cycles merges and enters the high-pressure turbine (T1) to perform work. It then passes through Heater 2 to absorb heat before entering T2 for expansion. This completes the thermodynamic cycle. The parameters designed for the system are listed in Table 1.

The modular design layout is adopted for the sCO_2 boiler, as shown in Fig. 1b. The length and flow rate of each heat exchange module are reduced to half of their original values. Since the frictional pressure drop follows $\Delta P_f \sim m^2 l$, the pressure drop (P_f) is reduced to 1/8. Represented by the red color, Heater 1 and Heater 2 operate in higher temperature region and supply heat to the top cycle, noting that Heater 2 also supplies heat to the bottom cycle. Represented by the blue color, Heater 4a and Heater 4b supply heat to the bottom cycle. The working fluid is split at point 4 and enters Heater 1, where it flows into module Part 1 and SH1, as well as Part 2 and SH2. Similarly, the flow is split at point 4′ and enters Heater 2, where it is distributed to LRH1 and HRH1, as well as LRH2 and HRH2. Due to the high heat flux density inside the furnace, CO_2 enters the cooling wall at a high temperature, making Part 1 and Part 2 more prone to overheating. Therefore, this study focuses on Part 1 and Part 2 of the cooling wall. To prevent overheating, Part 1 adopts a downward flow configuration using low-temperature working fluid to match the high heat flux.

The system operates under variational loads, ranging from 50 %THA to 100 %THA. The storage control method is used. The system

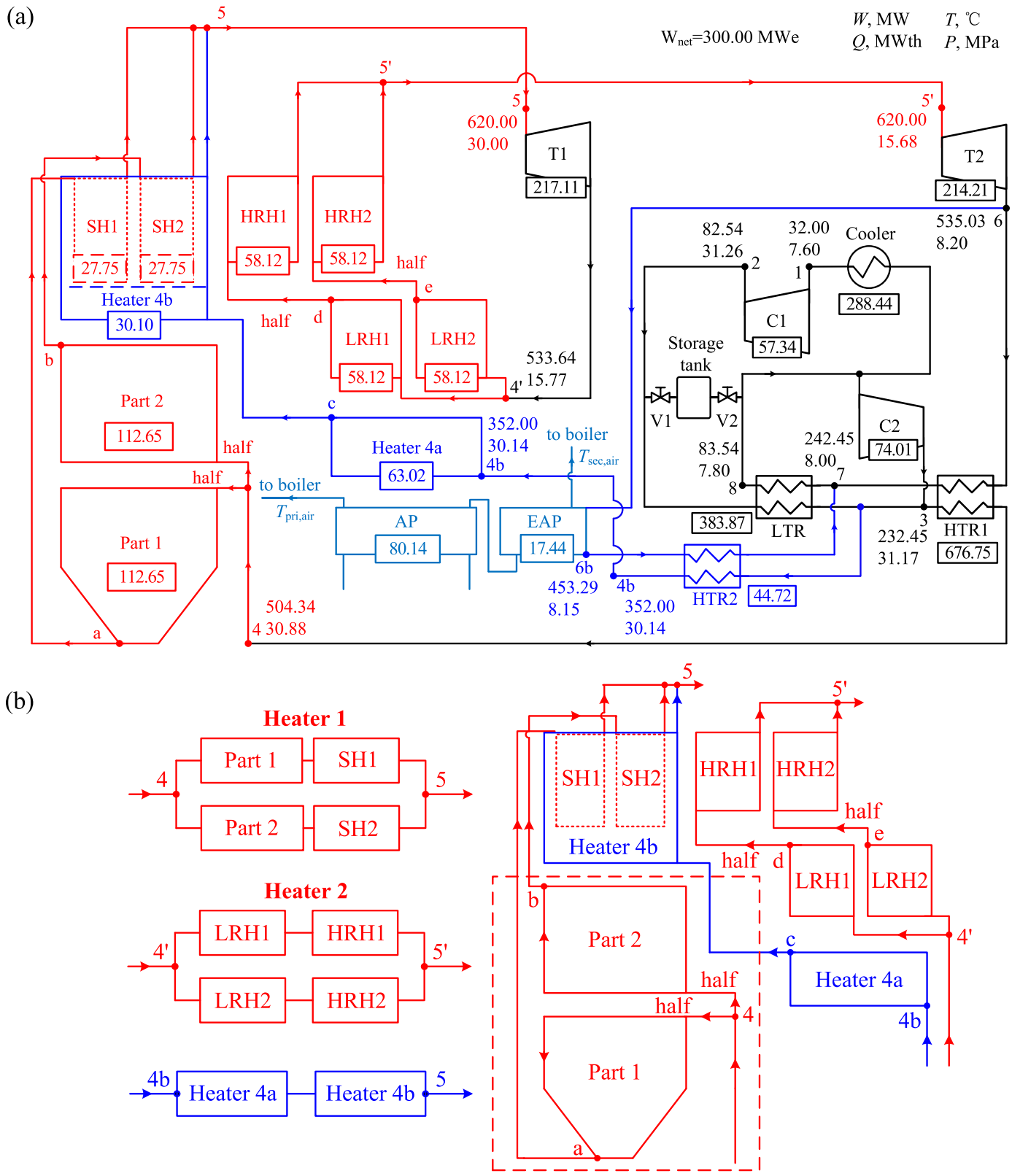


Fig. 1. sCO_2 coal-fired power generation system and modular sCO_2 boiler design.

incorporates a storage tank whose inlet, positioned at the outlet of the main compressor C1 (point 2 in system), is regulated by Valve 1. The tank outlet is situated at the cooler inlet (point 8 in system) and is controlled by Valve 2. The pressure difference between the storage tank and the main cycle is utilized to regulate CO_2 within the system. When the system load decreases, Valve 1 opens. CO_2 flows from the cycle into the storage tank, thereby reducing the CO_2 inventory within the system. When the system load increases, Valve 2 opens. CO_2 is released from the storage tank back into the cycle, increasing the system's CO_2 inventory. The design and off-design performance models for system components,

Table 1
Main parameters of sCO_2 cycle at rated condition.

State points	Pressure/MPa	Temperature/°C	Mass flow rate/t/h
1	7.60	32.00	5282.32
2	31.26	82.54	5282.32
3	31.17	232.45	6857.51
4	30.88	504.34	6857.51
4b	30.14	352.00	983.93
5	30.00	620.00	7841.45
4′	15.77	533.64	7841.45
5′	15.68	620.00	7841.45
6	8.20	535.03	7841.45
6b	8.15	453.29	660.32
7	8.00	242.45	7841.45
8	7.80	83.54	7841.45

along with the partial load calculation procedures, are detailed in Ref. [24].

As an example, the load increase process is used to illustrate the variations of main parameters, as shown in Fig. 2. The CO_2 flow rate at the cooling wall inlet (point 4 in system), denoted as $m_{CO2,4}$, increases from 4640.24 t/h to 6857.51 t/h. The corresponding temperature, $T_{CO2,4}$, decreases from 518.78 °C to 504.34 °C. The pressure $P_{CO2,4}$ increases from 21.58 MPa to 30.88 MPa. The average heat flux of furnace, q_{ave}, rises from 89.38 kW/m^2 to 147.14 kW/m^2. Three LVRs are considered: 2 % Pe/min, 5 % Pe/min, and 10 % Pe/min, corresponding to load increase completion time at 1500 s, 600 s, and 300 s, respectively. Due to operational constraints in applications, achieving an LVR of 10 % Pe/min is currently infeasible [25]. Therefore, the analysis of the 10 % Pe/min case is theoretical. The variations of main parameters during the simulation of load decrease process are the exact reverse of those during load increase process.

Among $m_{CO2,4}$, $T_{CO2,4}$, $P_{CO2,4}$ and q_{ave}, q_{ave} is dependent on the combustion intensity in the furnace. Variations of $m_{CO2,4}$, $T_{CO2,4}$, $P_{CO2,4}$ are dependent on dynamic characteristics of compressors, turbines, valves and pipelines. Indeed, these parameters are coupled with each other. In order to simplify the system modeling, these parameters can be decoupled by the control system [26]. In component-level studies, such treatment can be found in many articles [27,28]. The linear variation of these parameters is an assumption widely used by many investigators [28–30]. Previous studies on the Rankine cycle power plant using water-steam as the working fluid shows that the linear assumption can be approached by comparing with the operation data [30,31]. Thus, the linear assumption is also adopted here. To consider the deviation from the linear variation assumption, sensitivity analysis is performed by imposing the stepwise variation on the basis of the linear variation curve of the parameters with respect to time, see Section 4.2 for the outcomes.

3. Model and methods

The furnace model, the structural parameters of the cooling wall, and the heat load distribution along the furnace height direction are illustrated in Fig. 3. The boiler adopts π-type arrangement and four-corner tangential combustion configuration. The furnace has a square cross-section. Part 1 and Part 2 are 14.3 m and 14.1 m in height, respectively. The fin thickness (δ_w) of cooling wall is 6 mm. As the combustion configuration of a sCO_2 boiler is similar to that of a conventional water-steam boiler, the heat load distribution along the furnace height in Fig. 3c is based on [32]. The combustion process exhibits dynamic responses during load variation process. In Fig. 3d, the dashed line represents $\eta_{q,h}$ at 75 %THA, derived from the linear interpolation between the values at 50 %THA and 100 %THA, while the solid line indicates the actual $\eta_{q,h}$ at 75 %THA [32]. The two curves matched well, with the maximum deviation less than 10 %. Thus, the linear interpolation between 50 %THA and 100 %THA is employed as an approximation to simplify the combustion model. At each furnace height, the local heat flux is calculated by multiplying the average heat flux, q_{ave}, by the height-dependent thermal load distribution coefficient, $\eta_{q,h}$.

3.1. Numerical model

An unsteady fluid-solid coupling model is developed for a single tube in the sCO_2 boiler cooling wall. A one-dimensional flow model is

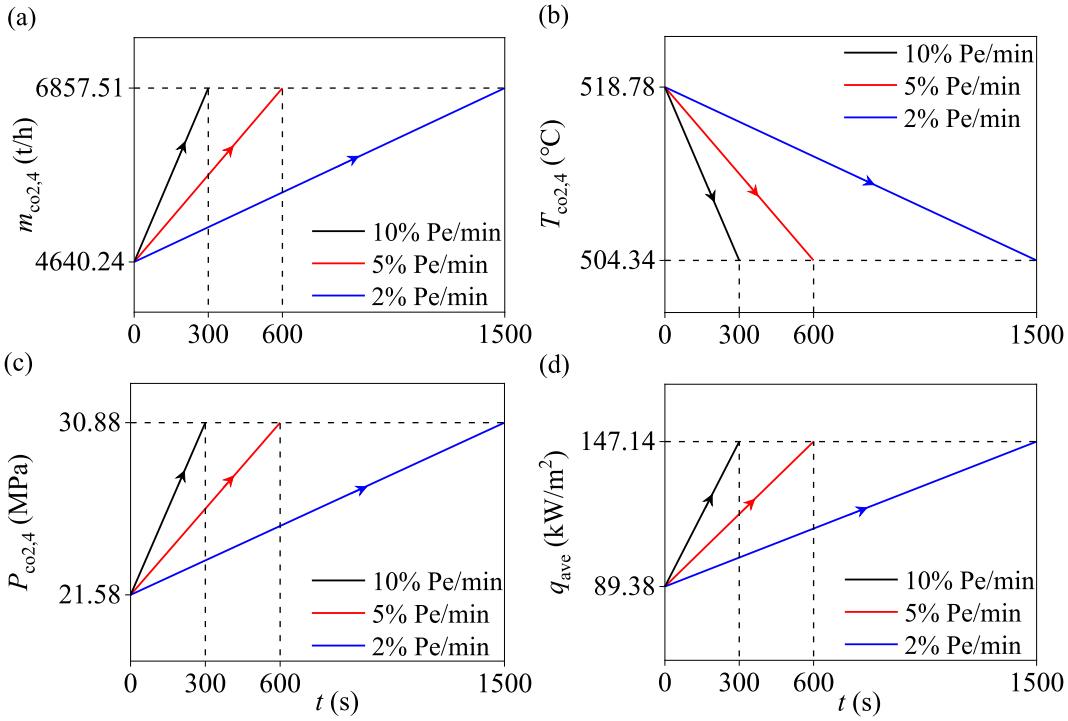


Fig. 2. Variations of main parameters during the load increase stage from 50 %THA to 100 %THA (a, b and c: CO_2 flow rate $m_{CO2,4}$, temperature $T_{CO2,4}$ and pressure $P_{CO2,4}$ at the boiler inlet, d: average heat flux of furnace q_{ave}).

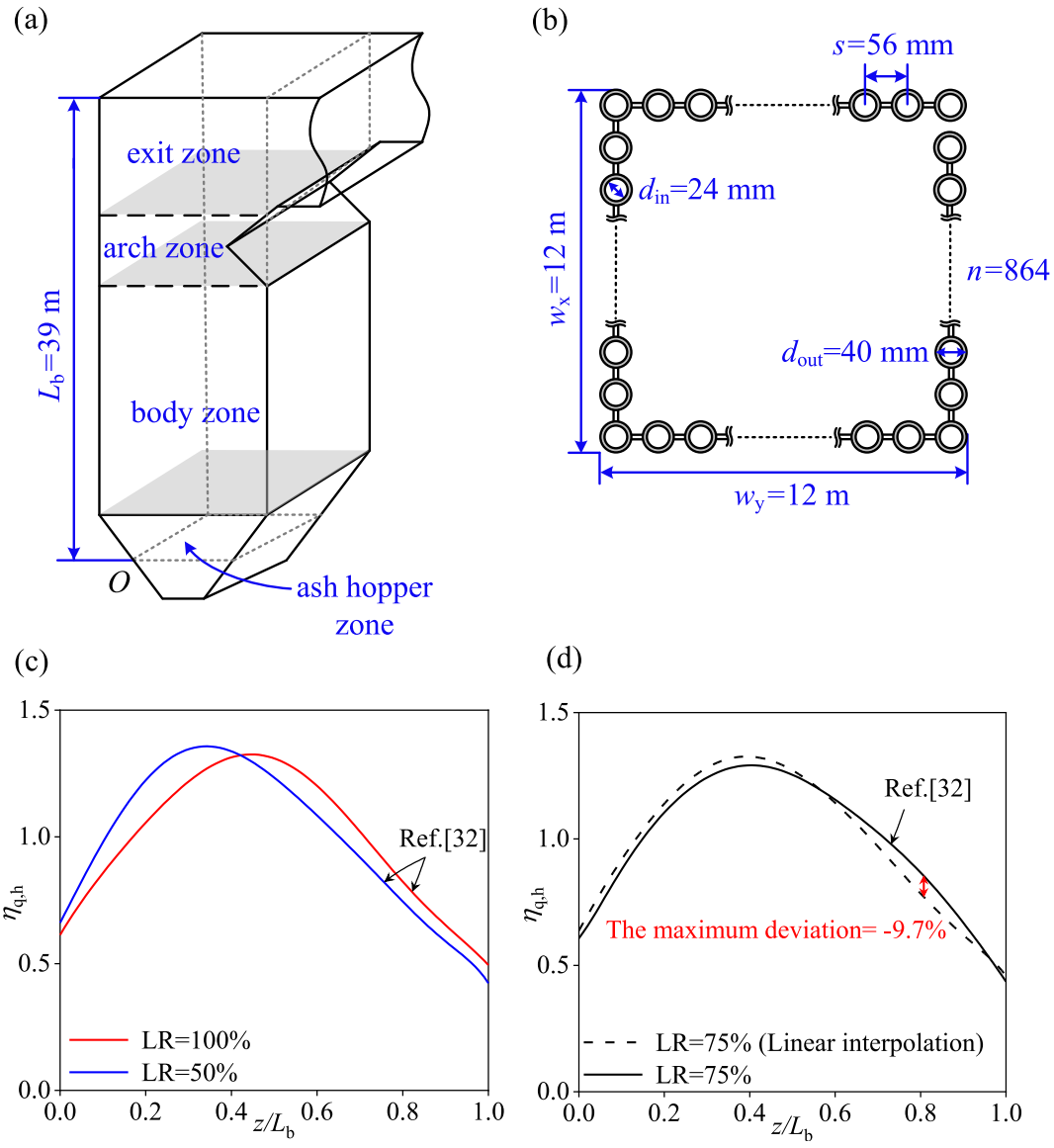


Fig. 3. The furnace model (a: 3D furnace, b: cross-section of the furnace, c: heat load distribution in the furnace height direction [32], d: linear interpolation and actual heat load distribution at 75 %THA).

employed to describe the internal fluid behavior. The flow and heat transfer are governed by the conservation equations of mass, momentum, and energy. The pipe wall is modeled as a two-dimensional domain. The governing equations are derived from the energy conservation principle. The membrane wall consists of vertical smooth tubes. The model is based on the following assumptions:

- Flow and thermal deviations among tubes are neglected.
- Axial heat conduction within the tube wall is neglected.
- Heat loss through the insulation layer of the membrane wall is neglected.

3.2. One-dimensional heat transfer model for the fluid domain

The one-dimensional flow and heat transfer of CO_2 inside the tube is solved using the following equations:

Mass conservation equation:

$$\frac{\partial \rho}{\partial t} = -\frac{1}{A}\frac{\partial m}{\partial z} \tag{1}$$

Momentum conservation equation:

$$\frac{\partial m}{\partial t} = -\frac{1}{A}\frac{\partial}{\partial z}\left(\frac{m^2}{\rho}\right) - A\left(\frac{\partial P}{\partial z} + \frac{\partial P_f}{\partial z} + \rho g \sin\beta\right) \tag{2}$$

Energy conservation equation:

$$\frac{\partial i}{\partial t} = \left(1 - \frac{1}{\rho}\frac{\partial P}{\partial i}\right)^{-1}\left[\frac{m}{A\rho}\left(\frac{1}{\rho}\frac{\partial P}{\partial z} - \frac{\partial i}{\partial z} + \frac{1}{\rho}\frac{\partial P_f}{\partial z}\right) + q_{in}\frac{U}{A\rho} - \frac{1}{A\rho}\frac{\partial P}{\partial \rho}\frac{\partial m}{\partial z}\right] \tag{3}$$

where m is the flow rate of CO_2 in a single tube, calculated as the total system flow rate divided by the number of cooling wall tubes. A denotes the cross-sectional flow area of the tube. i represents the specific enthalpy of the fluid. The heat flux, q_{in}, is determined from the tube wall energy balance, which will be discussed in the next section. The frictional pressure drop $\frac{\partial P_f}{\partial z}$ is evaluated using the Darcy-Weisbach equation [33]:

$$\frac{\partial P_f}{\partial z} = \frac{f}{d_{in}}\cdot\frac{\rho u^2}{2} \tag{4}$$

where the Darcy friction factor f is calculated using the following correlation [34]:

$$f=\frac{1}{3.24\lg^2\left[\left(\frac{\Delta/d_{in}}{3.7}\right)^{1.1}+\frac{6.9}{Re}\right]} \tag{5}$$

where Δ is the absolute roughness of the tube wall [35]. *Re* denotes the Reynolds number.

3.3. Two-dimensional heat transfer model for the tube wall

The blue shaped region in Fig. 4 represents the computational domain, which includes both the tube wall and the fin. The model is discretized into 24 control volumes per unit height, with each control volume associated with a representative node. Both radial and circumferential heat conduction are considered in the model. The energy conservation equations for several representative control volumes are given as follows [36,37]:

$$c_1\rho_1\frac{\Delta\widehat{\varphi}}{2}\left({r_{out}}^2-{r_{mi}}^2\right)\frac{dT_1}{dt}=k_1\frac{T_2-T_1}{\Delta\widehat{\varphi}r_{out}}\Delta r+k_1\frac{T_{24}-T_1}{\Delta r}\Delta\widehat{\varphi}r_{mi}+q_1\Delta\widehat{\varphi}r_{out} \tag{6}$$

$$c_3\rho_3\frac{\Delta\widehat{\varphi}}{2}\left({r_{out}}^2-{r_{mi}}^2\right)\frac{dT_3}{dt}=k_3\frac{T_2-T_3}{\Delta\widehat{\varphi}r_{out}}\frac{\Delta r}{2}+k_3\frac{T_4-T_3}{\Delta\widehat{\varphi}r_{out}}\frac{\Delta r}{2}+k_3\frac{T_{22}-T_3}{\Delta r}\Delta\widehat{\varphi}r_{mi}+q_3\Delta\widehat{\varphi}r_{out} \tag{7}$$

$$c_5\rho_5\frac{\Delta\widehat{\varphi}}{2}\left({r_{out}}^2-{r_{mi}}^2\right)\frac{dT_5}{dt}=k_5\frac{T_4-T_5}{\Delta\widehat{\varphi}r_{out}}\frac{\Delta r}{2}+k_5\frac{T_{10}-T_5}{\Delta\widehat{\varphi}r_{out}}\frac{\Delta r}{2}+k_5\frac{T_6-T_5}{\Delta x}\Delta\widehat{\varphi}r_{out}+k_5\frac{T_{20}-T_5}{\Delta r}\Delta\widehat{\varphi}r_{mi}+\frac{q_5\Delta\widehat{\varphi}r_{out}}{2} \tag{8}$$

$$c_6\rho_6\frac{\Delta x\delta_w}{2}\frac{dT_6}{dt}=k_6\frac{T_5-T_6}{\Delta x}\Delta\widehat{\varphi}r_{out}+k_6\frac{T_7-T_6}{\Delta x}\frac{\delta_w}{2}+k_6\frac{T_9-T_6}{\delta_w}\Delta x+q_6\Delta x \tag{9}$$

$$c_7\rho_7\frac{\Delta x\delta_w}{2}\frac{dT_7}{dt}=k_7\frac{T_6-T_7}{\Delta x}\delta_w+k_7\frac{T_8-T_7}{\delta_w}\Delta x+q_7\Delta x \tag{10}$$

$$c_8\rho_8\frac{\Delta x\delta_w}{2}\frac{dT_8}{dt}=k_8\frac{T_9-T_8}{\Delta x}\delta_w+k_8\frac{T_7-T_8}{\delta_w}\Delta x \tag{11}$$

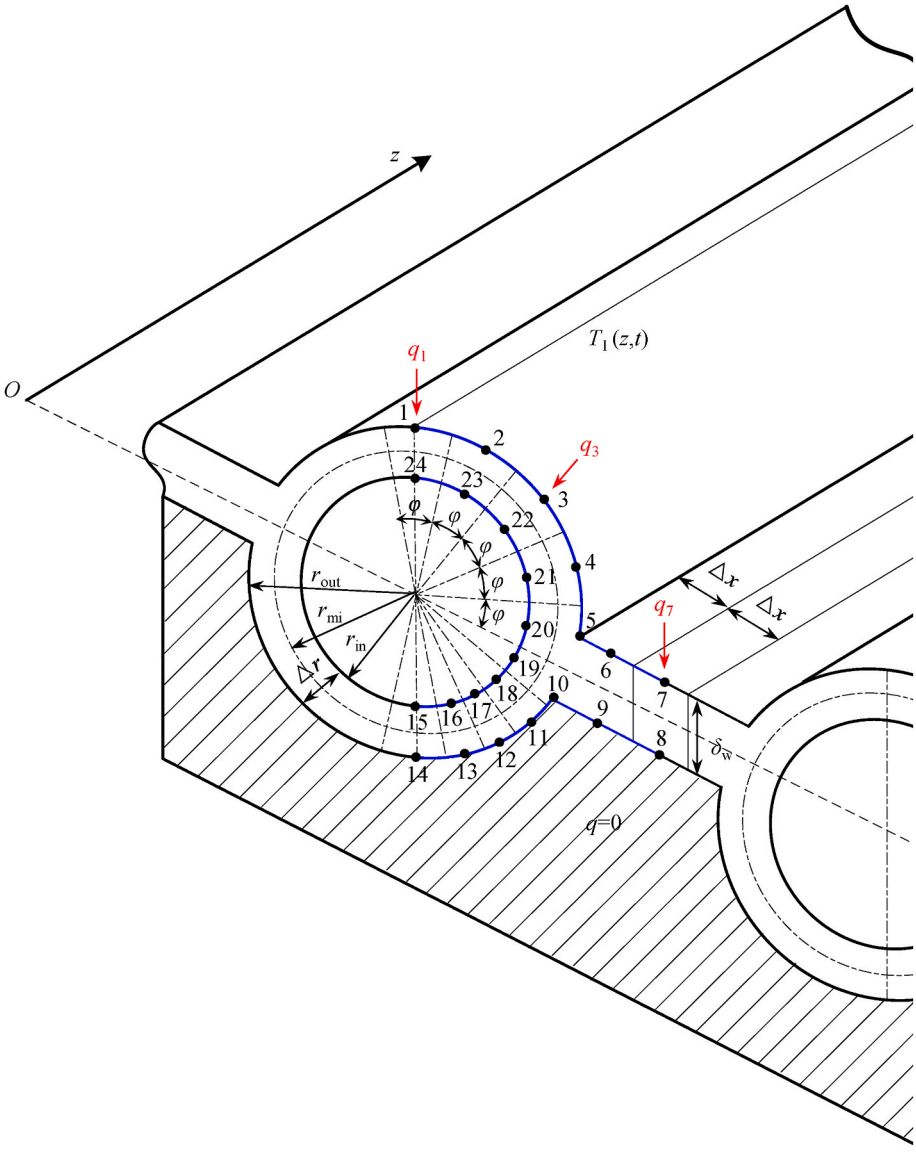


Fig. 4. Calculation model of the cooling tube wall.

$$c_9\rho_9\frac{\Delta x\delta_w}{2}\frac{dT_9}{dt}=k_9\frac{T_{10}-T_9}{\Delta x}\Delta\widehat{\varphi}r_{out}+k_9\frac{T_8-T_9}{\Delta x}\frac{\delta_w}{2}+k_9\frac{T_6-T_9}{\delta_w}\Delta x \quad (12)$$

$$c_{10}\rho_{10}\frac{\Delta\widehat{\varphi}}{2}\left(r_{out}{}^2-r_{mi}{}^2\right)\frac{dT_{10}}{dt}=k_{10}\frac{T_{11}-T_{10}}{\Delta\widehat{\varphi}r_{out}}\frac{\Delta r}{2}+k_{10}\frac{T_5-T_{10}}{\Delta\widehat{\varphi}r_{out}}\frac{\Delta r}{2}+k_{10}\frac{T_9-T_{10}}{\Delta x}\Delta\widehat{\varphi}r_{out}+k_{10}\frac{T_{19}-T_{10}}{\Delta r}\Delta\widehat{\varphi}r_{mi} \quad (13)$$

$$c_{22}\rho_{22}\frac{\Delta\widehat{\varphi}}{2}\left(r_{mi}{}^2-r_{in}{}^2\right)\frac{dT_{22}}{dt}=k_{22}\frac{T_{23}-T_{22}}{\Delta\widehat{\varphi}r_{in}}\frac{\Delta r}{2}+k_{22}\frac{T_{21}-T_{22}}{\Delta\widehat{\varphi}r_{in}}\frac{\Delta r}{2}+k_{22}\frac{T_3-T_{22}}{\Delta r}\Delta\widehat{\varphi}r_{mi}+\alpha_{22}\left(T_f-T_{22}\right)\Delta\widehat{\varphi}r_{in} \quad (14)$$

$$c_{24}\rho_{24}\frac{\Delta\widehat{\varphi}}{2}\left(r_{mi}{}^2-r_{in}{}^2\right)\frac{dT_{24}}{dt}=k_{24}\frac{T_{23}-T_{24}}{\Delta\widehat{\varphi}r_{in}}\Delta r+k_{24}\frac{T_1-T_{24}}{\Delta r}\Delta\widehat{\varphi}r_{mi}+\alpha_{24}\left(T_f-T_{24}\right)\Delta\widehat{\varphi}r_{in} \quad (15)$$

where c is the specific heat capacity, ρ is the density, k is the thermal conductivity, α is the convective heat transfer coefficient, T is the tube wall temperature, T_f is the temperature of the working fluid. r_{out}, r_{mi} and r_{in} represent the outer, mid, and inner radius of the tube, respectively. Δx is the spatial discretization step in the x-direction for the fin region. $\Delta\widehat{\varphi}=\frac{\pi\varphi}{180}$. q represents the local heat flux at a given height, obtained by multiplying the base heat flux with the angular coefficient ϕ corresponding to each control volume.

The inner wall heat flux, q_{in}, is determined based on the inner wall temperature T_{15}-T_{24} and the working fluid temperature T_f. It is averaged over the inner wall surface as follow:

$$q_{in}=\left[0.5\Delta\widehat{\varphi}\alpha_{24}\left(T_{24}-T_f\right)+\Delta\widehat{\varphi}\alpha_{23}\left(T_{23}-T_f\right)+\Delta\widehat{\varphi}\alpha_{22}\left(T_{22}-T_f\right)+\Delta\widehat{\varphi}\alpha_{21}\left(T_{21}-T_f\right)+\Delta\widehat{\varphi}\alpha_{20}\left(T_{20}-T_f\right)+\Delta\widehat{\varphi}\alpha_{19}\left(T_{19}-T_f\right)+\Delta\widehat{\varphi}\alpha_{18}\left(T_{18}-T_f\right)+\Delta\widehat{\varphi}\alpha_{17}\left(T_{17}-T_f\right)+\Delta\widehat{\varphi}\alpha_{16}\left(T_{16}-T_f\right)+0.5\Delta\widehat{\varphi}\alpha_{15}\left(T_{15}-T_f\right)\right]/\pi \quad (16)$$

The accuracy of cooling wall temperature prediction largely depends on the convective heat transfer coefficient inside the tube. It is noted that almost all of the heat transfer coefficients of sCO_2 are obtained under the steady condition [38,39]. Transient heat transfer coefficients are rarely reported in the literature. Steady heat transfer correlation is used to deal with the transient analysis of cooling wall temperatures. Reasonability of such treatment is commented as follows. Firstly, the variation of physical properties of sCO_2 is not large. Considering the boiler as a whole, the entering temperature is ~500 °C and the outlet temperature is ~620 °C, which are far beyond the pseudo-critical temperature of (70–90) °C corresponding to the operation pressure of (20–30) MPa. Under such circumstance, the crossing of the pseudo-critical temperature does not take place to avoid the sharp crossing, and the variation of physical properties is weak in the temperature range of (500–620) °C. Secondly, the heat transfer process coupling the furnace side, the tube wall and the CO_2 fluid can be characterized by the diffusion time of the tube wall thickness [40], which is written as $\tau = L^2/\alpha$, where L is the characteristic length, equals to the tube wall thickness here, α is thermal diffusivity of the tube wall. Such time scale is estimated as (12–13) s covering the present data range, which is one to two magnitudes shorter than the time scale of (300–1500) s for the load variation process. This time scale difference allows the tube wall to adjust promptly to changing conditions.

The selection of heat transfer coefficient is important to ensure the correct prediction of cooling wall temperatures. Available heat transfer coefficients are developed considering the buoyancy and acceleration effects, causing large deviation from the experimental data [41,42]. A series of works have been done to improve the accuracy of the heat transfer coefficients. Additional experimental data of sCO_2 were achieved by establishing a high pressure-temperature convection loop, with the pressure up to 21 MPa, which is three times of the critical pressure of CO_2. Based on the heat transfer mechanism dominated by the wall attached vapor-like layer thickness, the dimensionless K number is proposed to characterize the competition between evaporation induced momentum force and inertia force to quantify the vapor-like layer effect. Hence, a general heat transfer correlation is developed, incorporating the K term, except the Reynolds number and the Prandtl number [43]. Totally 5560 data points are involved to develop the heat transfer correlation, comprising 2028 data points from our own experiments and 3532 data points cited from 18 open literatures, involving three working fluids of CO_2, H_2O, and R134a. Zhu et al. [43] compared the Nusselt number (Nu) and inner wall temperature predicted by the K number correlation with predictions using five correlations of Bishop et al. [44], Jackson [45], Jackson and Hall [46], Yu et al. [47], Gupta et al. [48]. Fig. 5 summarizes the error indexes among the six correlations, including the mean relative error (e_A), mean absolute relative error (e_R), and root-mean-square error (e_S). For all three working fluids, the K number correlation presents the highest accuracies, demonstrating a clear advantage using the K number correlation. The detailed expressions are given as follows:

$$\alpha=\frac{Nu\cdot k_f}{d_{in}} \quad (17)$$

where k_f is the thermal conductivity of the working fluid. The Nusselt number, Nu, is calculated as follows:

$$Nu=0.0012Re_f^{0.9484}Pr_{f,ave}^{0.718}K^{-0.0313} \quad (18)$$

$$Re_f=\frac{G\cdot d_{in}}{\mu_f},Pr_{f,ave}=\frac{\mu_f\cdot c_{ave}}{k_f},c_{ave}=\frac{i_{wi}-i_f}{T_{wi}-T_f} \quad (19)$$

where Pr denotes the Prandtl number. The subscript f indicates that the thermophysical properties are evaluated using the working fluid temperature as the reference temperature, and the subscript ave denotes the average value. G represents the mass velocity. μ is the dynamic viscosity. The subscript wi indicates that the properties are evaluated using the inner wall temperature.

The supercritical K number is calculated as follow:

$$K=\left(\frac{q_{in}}{G\cdot i_{wi}}\right)^2\frac{\rho_f}{\rho_{wi}} \quad (20)$$

Owing to the high temperature of the sCO_2 boiler cooling wall, Super304H (10Cr18Ni9NbCu3BN) is selected as the wall material. High temperature corrosion can cause thinning of tube walls and may even lead to rupture of the heated surfaces, endangering the safe operation of the unit. The maximum allowable temperature of Super304H determined by the corrosion limit is 705 °C.

3.4. Calculation procedure

The calculation procedure for transient load variation process is illustrated in Fig. 6. Firstly, the thermodynamic cycle parameters and boiler design parameters are provided as input. The integrated design process for the sCO_2 coal-fired power generation system and its components is then executed. The geometric parameters of each heater module, the inlet parameters of the cooling wall and the q_{ave} in the furnace under the rated condition are obtained. Subsequently, the partial load calculation procedure for sCO_2 coal-fired power generation system [24] is executed. The corresponding inlet parameters and q_{ave} at 50 %THA are obtained. The above simulations are performed in MATLAB.

Finally, the unsteady fluid-solid coupling model is developed using Aspen Custom Modeler (ACM). Thermophysical properties of CO_2 are obtained from the built-in property database in Aspen. For Super304H, the metal density (ρ) is not changed versus temperature, which is 7940 kg/m^3. Thermal conductivity (k) and specific heat capacity (c) are given in Table 2 at various temperatures, which are used to yield following

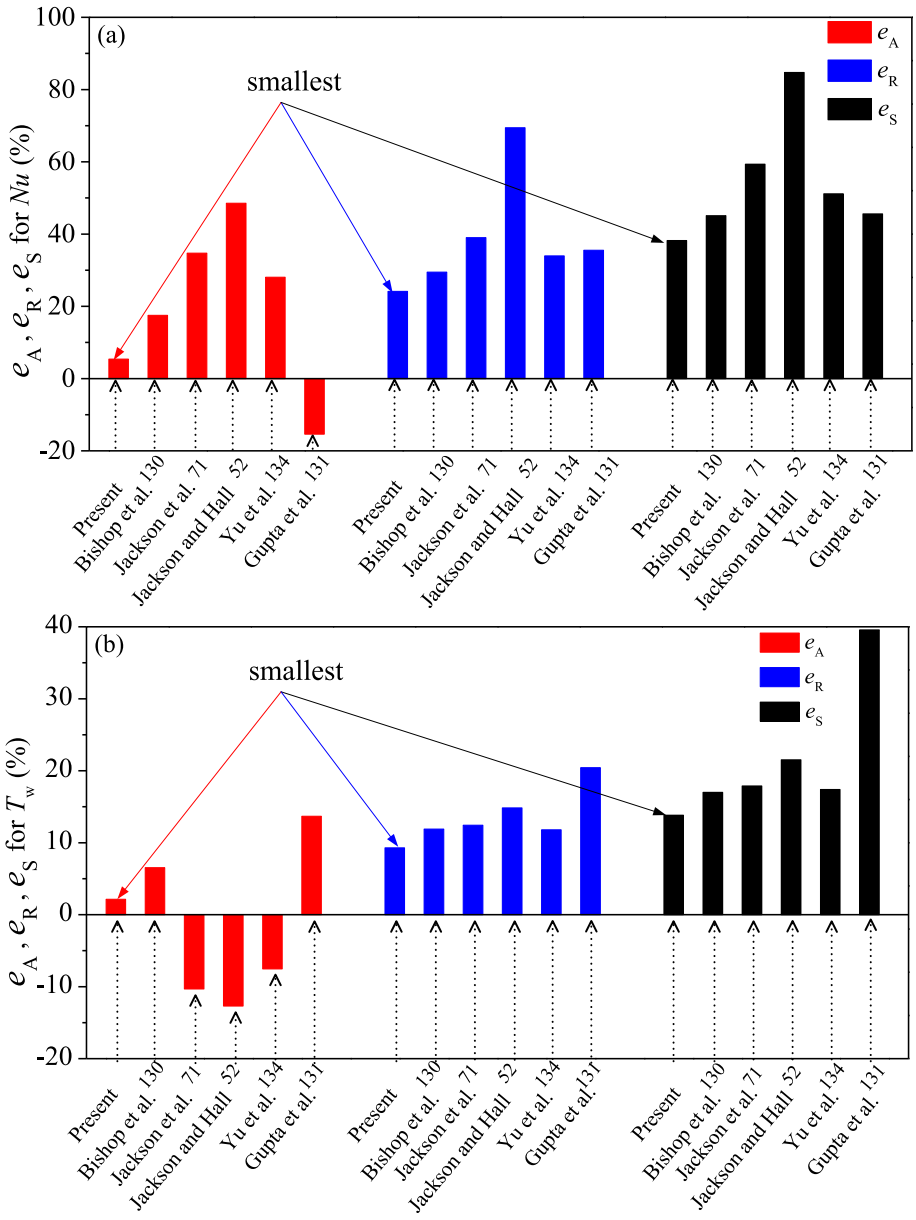


Fig. 5. Summary of the mean error e_A, mean absolute error e_R and square-root error e_S for Nusselt number and inner wall temperatures at given heat fluxes conditions [43], Copyright 2020, Elsevier.

correlations (for 500–700 °C):

$$k = 10.7 + 0.029T \tag{21}$$

$$c = \left(-244.53 + 2.83T - 0.002043T^2 \right) / 10^3 \tag{22}$$

where the units of k, c and T are W/(m·K), kJ/(kg·K) and °C, respectively. The initial conditions at $t = 0$ are set with the parameters corresponding to 50 %THA and 100 %THA conditions, respectively. The boundary conditions of $m_{CO2,4}$, $T_{CO2,4}$, $P_{CO2,4}$ and q_{ave} are expressed in Fig. 2. By applying these parameters over specific time intervals, transient thermal behavior of cooling wall tubes under different LVRs are numerically simulated. The model is solved using a variable step size implicit Euler method. The minimum and maximum time steps are set to 0.001 s and 0.5 s, respectively. The first-order backward finite difference (BFD1) method is employed for discretization. Part 1 and Part 2 are discretized into 29 cross-sections along the z direction, respectively. To ensure the prediction accuracy, the effect of discretization size in the height direction on prediction outcomes are conducted. The four subfigures of Fig. 7 show the temperature T_1 at 2 m beyond the entrances of Part 1 (Fig. 7a) and Part 2 (Fig. 7b), at the outlets of Part 1 (Fig. 7c) and Part 2 (Fig. 7d), respectively. Totally 15, 29 and 57 cross-sections are divided in the furnace height, corresponding to the mesh sizes of $\Delta z \approx 1$ m, 0.5 m and 0.25 m, respectively. It is seen that the three curves using three different mesh sizes show very small difference. The following figures are presented using $\Delta z \approx 0.5$ m with 29 cross-sections in the height direction.

3.5. Model validation

Since the 300 MW sCO_2 coal-fired boiler is not yet in operation, the model is validated against data from Ref. [36]. The plane view of the cooling wall is shown in Fig. 8a. The flow rate in the single cooling wall tube is 0.821 kg/s, with the inlet temperature of 315 °C and the inlet pressure of 29.9 MPa. The tube diameter d_{out} and thickness Δr are 33.7 mm × 6.3 mm below the furnace height of 49.4 m, and 38.0 mm × 6.3 mm above that height. First, the steady state model is validated. The

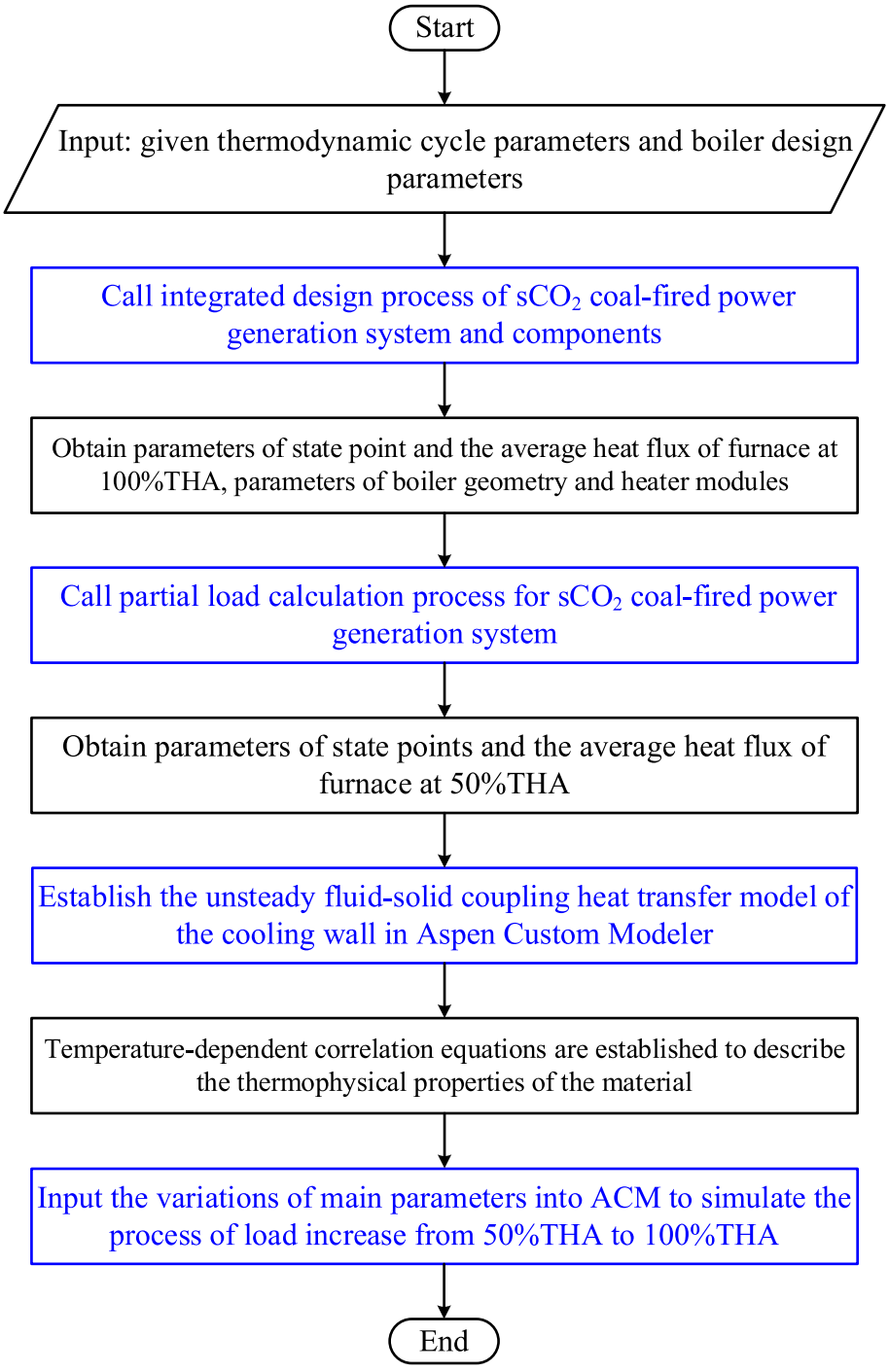


Fig. 6. The calculation procedure for transient load variation process.

Table 2
Physical properties of Super304H.

T/°C	100	300	500	600	700	800
thermal conductivity/ W/(m·K)	16.2	21.5	25.2	28.6	31	31
specific heat capacity/kJ/ (kg·K)	0.511	0.618	0.658	0.716	0.733	0.707

steady state temperature distributions along the tube length are shown in Fig. 8b. The simulation results show good agreement with the reference data. Next, the transient model is validated. Fig. 8c shows the temperature at the center of the fire-facing side of the tube wall T_1, and Fig. 8d shows the fin temperature T_5. These temperatures are recorded starting at $t = 0$ s by applying heat fluxes varying along the combustion chamber height. The maximum deviation of T_5 between the present predictions and the data from Ref. [36] is 1.87 %, indicating sufficient accuracy of the transient modeling.

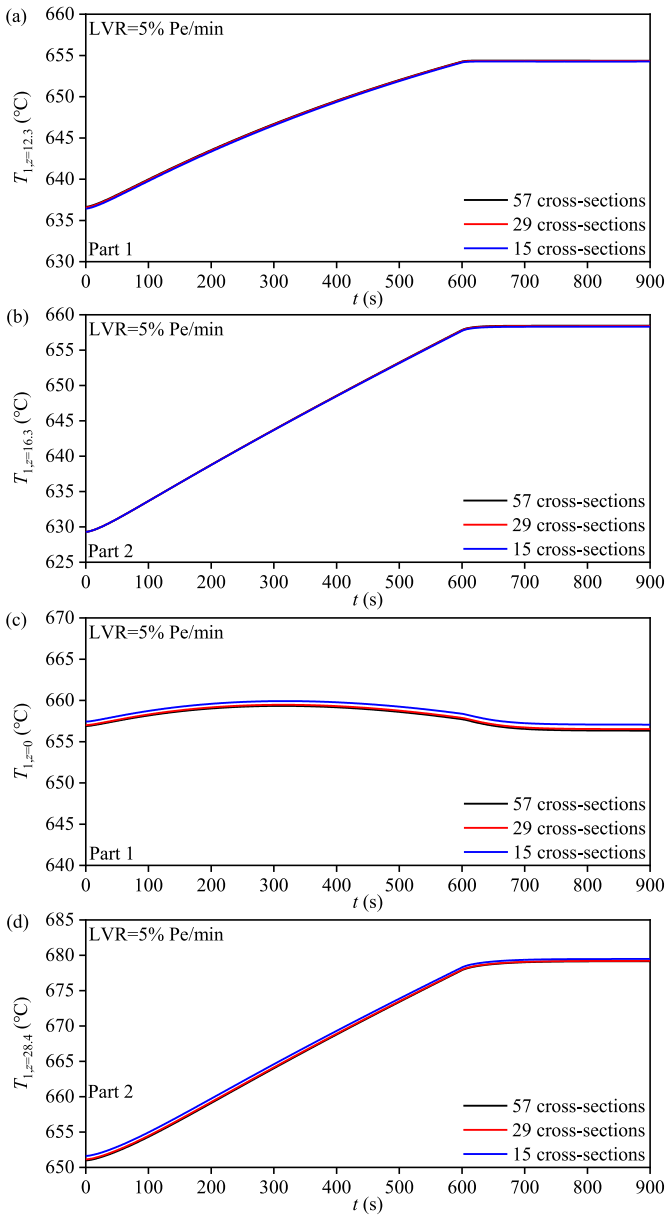


Fig. 7. Mesh independence study.

4. Results and discussion

Fig. 9 shows temperatures of the cooling wall and the fluid in the height direction at the load ratio of 50 %, noting the downward flow for Part 1 and upward flow for Part 2. As shown in the icon of Fig.9, T_1, T_{24} and T_7 are the temperatures at the outer tube ridge, the inner tube ridge, and the fin center. T_f represents the fluid temperature of CO_2. For Part 2, monotonic increase of T_1, T_7 and T_{24} are observed along the height direction. On the contrary, for Part 1, non-monotonic variations of these temperatures exist. Instead, these temperatures show the parabolic distribution. For both Part 1 and Part 2, T_f increases along the flow direction. The non-monotonic and monotonic variations of temperatures in Part 1 and Part 2 are caused by the heat flux distribution in the furnace height direction. The maximum temperature is 666.0 °C for Part 1 and 651.1 °C for Part 2.

4.1. Load increase process

To investigate the transient cooling wall temperatures during load changes, particular attention is first given to whether the temperatures exceed the material allowable temperature limit. Fig. 10 shows the hot spot temperatures of cooling wall during load increase from 50 %THA to 100 %THA under three LVRs of 2 % Pe/min, 5 % Pe/min, and 10 % Pe/min. The hot spot temperature means the highest temperature at any time. In Part 1, the hot spot temperature initially increases and then decreases under different LVRs. This phenomenon results from the competing effects between the increasing heat flux q and the combined influence of decreasing inlet temperature $T_{CO2,4}$ and increasing inlet mass flow rate $m_{CO2,4}$ during the load increase process. The CO_2 inside the cooling wall is far from the pseudo-critical point. The inlet pressure $P_{CO2,4}$ has a weak influence on wall temperature variation. Therefore, the effects of q, $T_{CO2,4}$ and $m_{CO2,4}$ on wall temperature are mainly analyzed below. After the load increase process ends, the hot spot temperature in Part 1 continues to decrease. A higher LVR leads to a larger deviation between the hot spot temperature at 100 %THA and the final stabilized value. At the LVR of 10 % Pe/min, it ultimately drops by 1.7 °C. This is attributed to the finite heat capacity of both the tube wall and the fluid. Due to thermal inertia, heat transfer between the tube wall and the fluid remains unbalanced even after the boundary conditions have stabilized. The tube wall continues to transfer heat to the fluid until thermal equilibrium is reached. In Part 1, the maximum hot spot temperatures during load increase process are 669.6 °C, 670.0 °C, and 670.5 °C at LVRs of 2 % Pe/min, 5 % Pe/min, and 10 % Pe/min, respectively.

The hot spot temperature in Part 2 exhibits an increasing trend during the load increase process. This is because the positive effect of increased q on wall temperature outweighs the negative effects of decreased $T_{CO2,4}$ and increased $m_{CO2,4}$. The hot spot temperature continues to rise after the load reaches 100 %. At the LVR of 10 % Pe/min, it ultimately increases by 2.2 °C. The maximum hot spot temperature reaches 681.4 °C at all the three LVRs, representing the stabilized value at the final state. During the load increase process, the hot spot temperatures in Part 1 and Part 2 remain below the temperature limit of the material.

In addition to hot spot temperature, the location of the hot spot also warrants attention. As shown in Fig. 11, L_{cw} denotes the total height of Part 1 and Part 2. The location z/L_{cw} represents the relative height of the hot spot within the cooling wall. In Part 1, the hot spot location exhibits a gradual upward shift during load increase process, with a small overall change. It increases from $z/L_{cw} = 0.16$ and eventually reaches $z/L_{cw} = 0.20$. This behavior may be attributed to the downward flow configuration in Part 1, where CO_2 enters from the top. As $T_{CO2,4}$ decreases and $m_{CO2,4}$ increases, the heat transfer capability in the upper region of Part 1 is enhanced with the rising heat flux. Additionally, the peak of the vertical heat flux distribution $\eta_{q,h}$ along the furnace height corresponding to Part 1 also shifts upward. As a result, more heat is absorbed in the upper region, causing the hot spot location to shift upward.

In Part 2, the hot spot location exhibits a rapid downward shift during the load increase process. It decreases from the initial position at $z/L_{cw} = 1.0$ (the outlet of Part 2) to $z/L_{cw} = 0.86$. This may be attributed to the upward flow in Part 2, where CO_2 enters from the bottom. As $T_{CO2,4}$ decreases and $m_{CO2,4}$ increases, the CO_2 in the lower region of Part 2 becomes more effective in absorbing heat. This leads to a downward shift in the hot spot location. Moreover, different LVR shows no significant influence on the variation of hot spot location in either Part 1 or Part 2.

The hot spot location along the cooling wall height has been analyzed. Next, the circumferential location of the hot spot is discussed. Fig. 12 shows the cross-sectional isothermal wall temperature curves at the cooling wall outlet at LVR = 5 % Pe/min for Part 1 and Part 2. The selected time points are $t = 0$ s, $t = 450$ s, and $t = 900$ s, corresponding to the initial state, intermediate state, and final stabilization state, respectively. During the load increase process, the hot spot at the outlet of Part 1 and Part 2 consistently appears at the center of the fire-facing side of the tube. These results indicate that the hot spot shifts exclusively

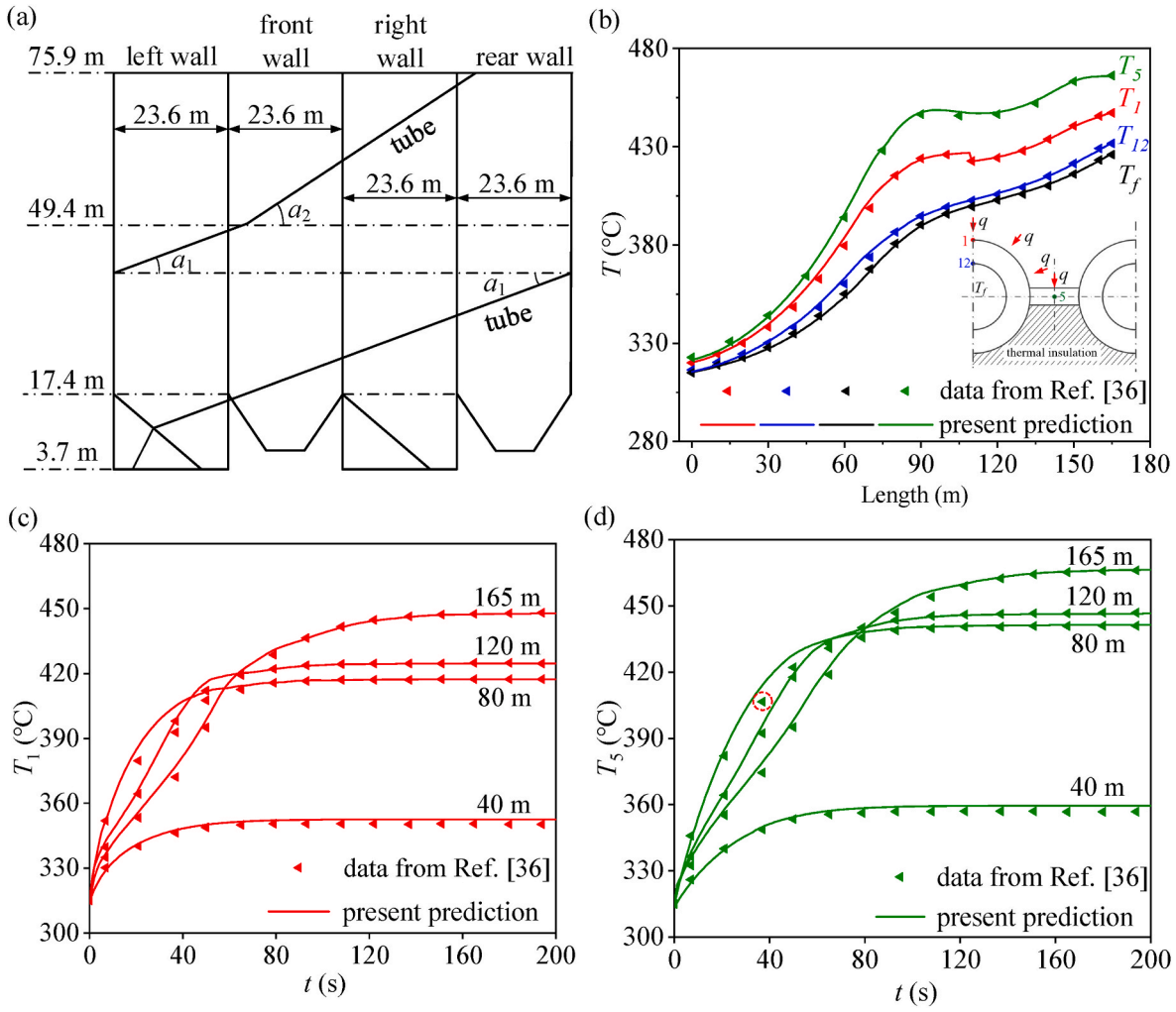


Fig. 8. Validation of the model calculations by comparing with the data from Ref. [36] (a: plane view of the four stretched cooling walls, b: cooling wall temperatures at the three specific locations and fluid temperatures along the tube length at the rated condition, c and d: variations of T_1 and T_5 versus time by suddenly applying heat flux on the tube at $t = 0$ s).

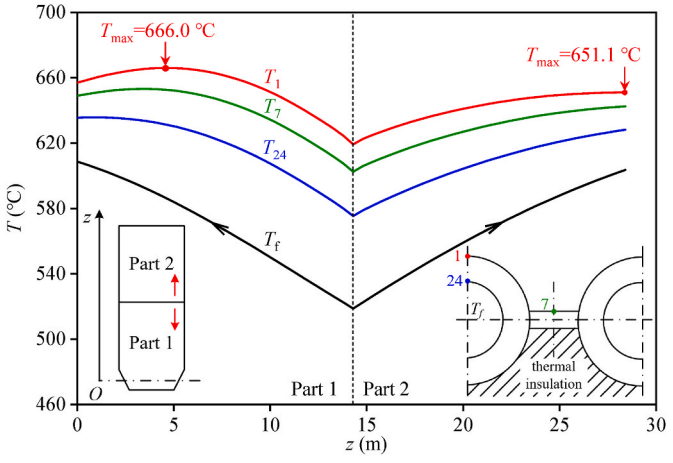


Fig. 9. Cooling wall temperatures and fluid temperatures along height direction at the load ratio of 50 %, noting downward flow for Part 1 and upward flow for Part 2.

along the height direction at point 1 (see Fig. 4).

As previously discussed, the maximum hot spot temperature reached under different LVRs are not identical. The impact of LVR on the maximum hot spot temperature is analyzed below. As shown in Fig. 13, max $(T_1^{\varphi,t})$ represents the maximum temperature on the tube wall during the load increase process, until thermal equilibrium is reached. In Part 1, max $(T_1^{\varphi,t})$ increases quasi-linearly with the increasing LVR. At the LVR of 1 % Pe/min, max $(T_1^{\varphi,t})$ is 669.5 °C. At 5 % Pe/min, it increases to 670.0 °C. At 10 % Pe/min, it reaches 670.5 °C. This phenomenon can be attributed to the fact that a higher LVR leads to a faster rate of heat flux input. Although the fluid also enhances heat absorption, the wall temperature T_1 responds more rapidly to the heat flux input. The tube wall accumulates more heat in a shorter time, leading to an increase in max $(T_1^{\varphi,t})$ with the rising LVR. In Part 2, max $(T_1^{\varphi,t})$ remains constant at different LVRs, with the value of 681.4 °C. This is because max $(T_1^{\varphi,t})$ in Part 2 corresponds to the final stabilized temperature, which is independent of LVR.

To consider the non-uniform effect, the circumferential non-uniformity coefficient ($\eta_{q,c}$) is introduced, in which $\eta_{q,c} = 1$, 1.1 and 0.9 represent the base value, a value 10 % higher than the base value and a value 10 % lower than the base value, respectively. The temperatures with the three non-uniform factors show a similar trend with respect to LVRs. The temperatures with $\eta_{q,c} = 1.1$ are ~15 K and ~17 K higher than those with $\eta_{q,c} = 1$ for Part 1 and Part 2, respectively. However, these temperatures are still lower than the temperature limit of 705 °C for Super304H. The lower non-uniform degree of $\eta_{q,c} = 0.9$ decreases the temperatures, which is beneficial for safe operation of the sCO_2 boiler.

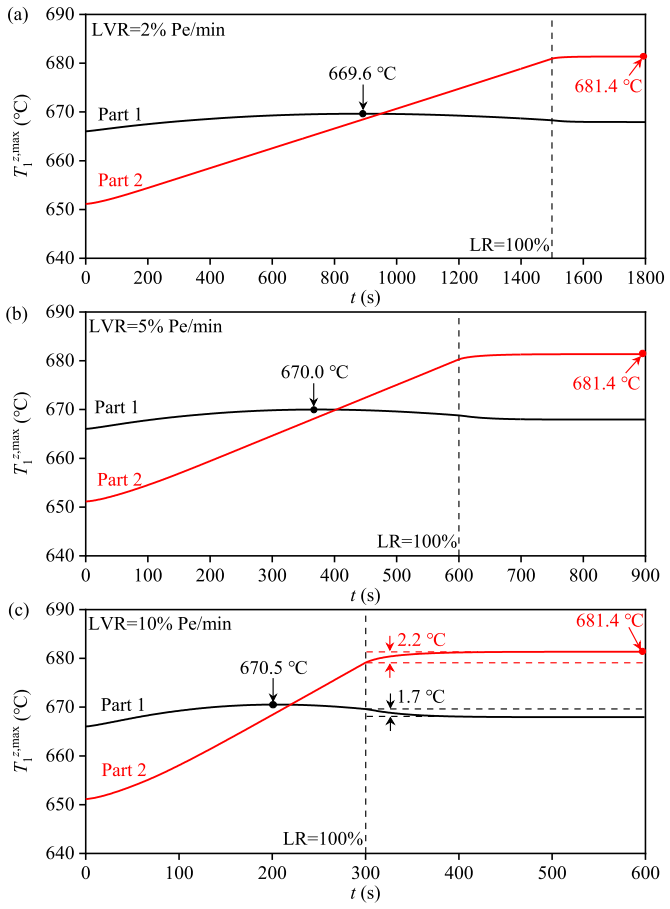


Fig. 10. Hot spot temperatures of cooling wall from 50 %THA to 100 %THA at three load variation rates of (a) LVR = 2 % Pe/min, (b) LVR = 5 % Pe/min, and (c) LVR = 10 % Pe/min.

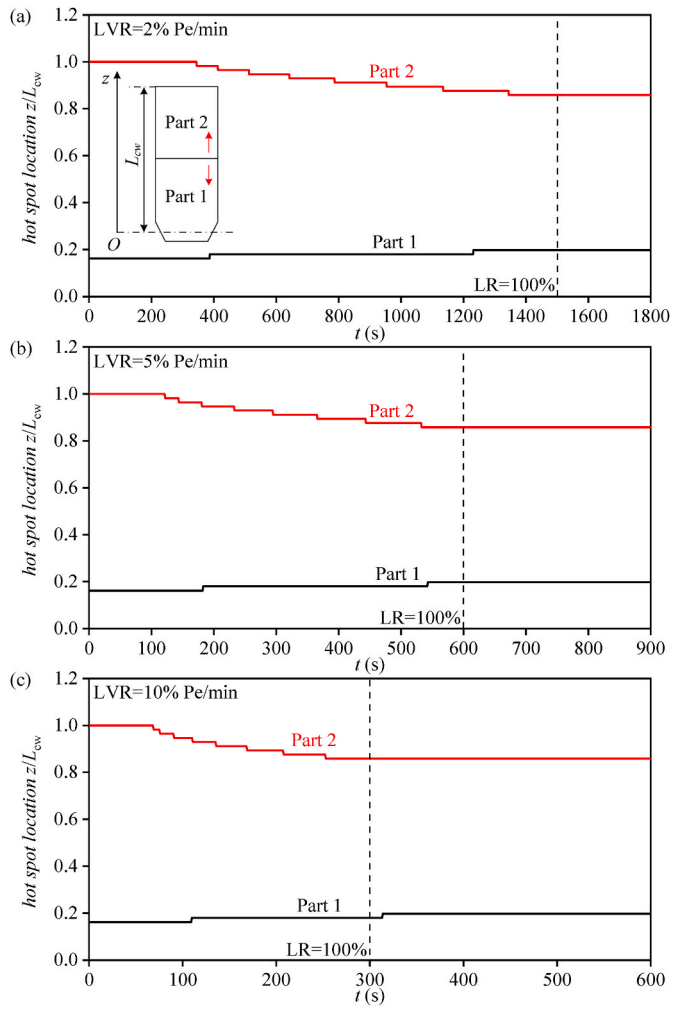


Fig. 11. The hot spot location z/L_{cw} versus time from 50 %THA to 100 %THA at load variation rates of (a) LVR = 2 % Pe/min, (b) LVR = 5 % Pe/min and (c) LVR = 10 % Pe/min.

To deal with transient heat transfer process of thermal system, the hot spot temperature and the temperature change rate are among the most important indexes. The rate of temperature change directly governs the magnitude of internal temperature gradients, which in turn drives the development of thermal stresses and potential thermal fatigue [49]. During startup, shutdown, or rapid load changes, significant temperature gradients can develop within components. When the temperature changes too rapidly, the finite thermal conductivity of materials results in non-uniform temperature fields, leading to thermal stresses through two primary mechanisms: Firstly, through-thickness temperature gradients, where the outer surface heats or cools more rapidly than the interior, producing differential expansion and internal stresses. Secondly, in-plane temperature non-uniformities, where different regions expand at different rates, causing bending and local stress concentrations. To mitigate these risks, it is essential to define a controlled temperature change rate. This allows sufficient time for thermal diffusion and stress relaxation, effectively reducing stress gradients and preventing structural damage such as plastic deformation or fatigue failure. Strict compliance with the temperature ramp-up criteria is therefore vital to avoid thermal stress-related failures and to ensure long-term, safe operation of thermal systems [25,50].

Due to above reasons, the temperature change rate is widely adopted as a control parameter for limiting thermal stress in the fields of electronic packaging [51], aerospace thermal management [52], and power engineering [53]. The critical temperature change rate is an important indicator for assessing the magnitude of thermal stress. A strict limit of 5 K/min, reported in the open literature, has been adopted in sCO_2 Brayton cycle systems as a safeguard against excessive thermal stresses [54,55]. Hence, in this study, the 5 K/min is adopted as a strict criterion, serving as a conservative alternative to thermal stress analysis.

Fig. 14a presents the temperature change rates of the control volume exhibiting the largest temperature variation with time in Part 1 and Part 2 under the three LVRs at $\eta_{q,c} = 1$. The temperature change rates of both Part 1 and Part 2 show a trend of first increasing and then decreasing with time. In Part 1, the temperature change rates remain below 5 K/min at LVR of 2 % Pe/min and 5 % Pe/min. At the LVR of 10 % Pe/min, the temperature change rate peaks at 4.9 K/min in the second minute before decreasing, remaining within the limit. In Part 2, at the LVR of 10 % Pe/min, it exceeds the limit at the second minute. Therefore, the LVR of 10 % Pe/min is not acceptable with respect to the temperature change rate limit of the pipe wall.

For practical operation, it is important to determine the critical LVR that satisfies the 5 K/min limit, which can be done by crossing the 5 K/min limit line with the max(dT/dt) ~ LVR curve. As shown in Fig. 14b, max(dT/dt) represents the maximum wall temperature change rate during the load increase process. It can be observed that max(dT/dt) in both Part 1 and Part 2 increases quasi-linearly with increase of LVR. In Part 1, max(dT/dt) remains below the criterion even at the LVR of 10 % Pe/min when $\eta_{q,c} = 0.9$ or 1. When $\eta_{q,c} = 1.1$, however, the criterion is reached at the LVR close to 9 % Pe/min. In Part 2, the intersection between max(dT/dt) and the criterion occurs earlier. Specifically, for $\eta_{q,c} = 0.9$, the intersection point lies at LVR of 8.04 % Pe/min; for $\eta_{q,c} = 1$, it occurs at 6.98 % Pe/min; and for $\eta_{q,c} = 1.1$, the criterion is met at 6.21 % Pe/min. Therefore, considering the temperature change rate limitation

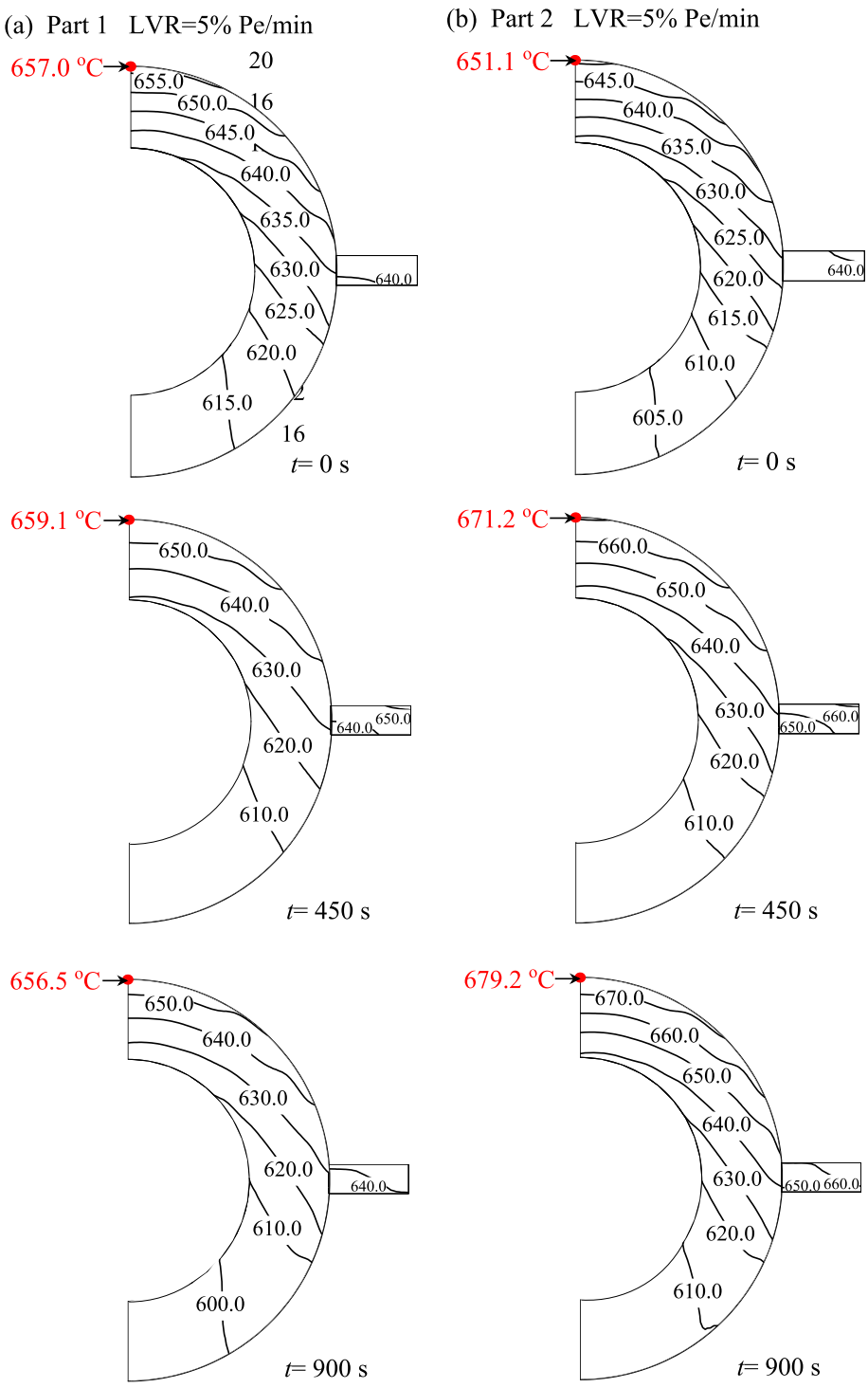


Fig. 12. The cross-sectional isothermal wall temperature curves at the cooling wall outlet at LVR = 5 % Pe/min for the Part 1 (a) and the Part 2 (b).

of the tube wall under circumferential heat flux non-uniformity, the maximum allowable LVR during the load increase process in this study is determined to be 6.21 % Pe/min.

4.2. Load decrease process

The boundary condition changes during the simulation of load decrease process are exactly opposite to those during the load increase process. Fig. 15 shows the hot spot temperatures of cooling wall at LVR of −2 % Pe/min, −5 % Pe/min, and −10 % Pe/min under $\eta_{q,c} = 1$. Under different LVR, the hot spot temperature in Part 1 exhibits a trend of initial decrease, followed by a slight increase, and then a subsequent decrease. After the load decreases to 50 %, the hot spot temperatures continue to decline slightly before stabilizing. Similar to the load increase process, the wall temperature response during load decrease is also governed by the competing positive and negative effects of boundary condition changes on the pipe wall. In Part 1, the maximum hot spot temperatures are 669.1 °C, 668.7 °C, and 667.9 °C at LVR of −2 % Pe/min, −5 % Pe/min, and −10 % Pe/min, respectively. The maximum hot spot temperature decreases with increase of |LVR|. This can be attributed to the fact that T_1 responds more rapidly to the reduction of heat flux, leading to greater heat loss from the tube wall. In

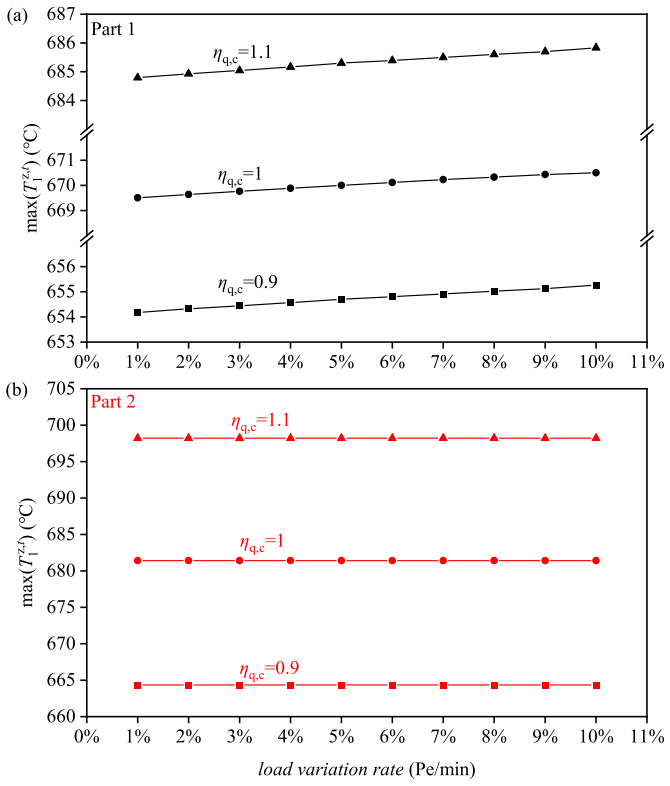


Fig. 13. Effect of load variation rates on the hot spot temperatures of cooling wall.

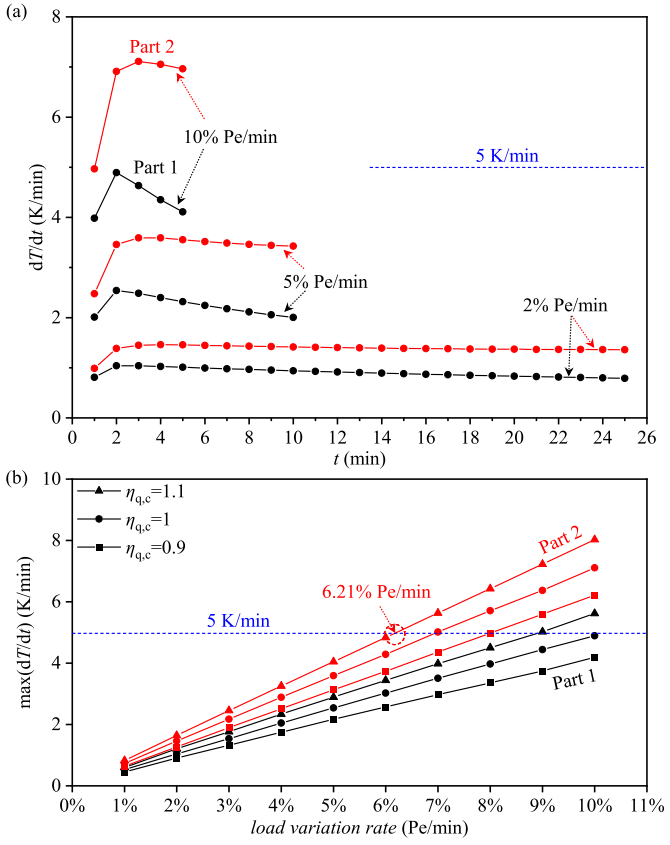


Fig. 14. Effect of load variation rates on temperature change rates of cooling wall (a: temperature change rates versus time, b: quasi-linear distribution of maximum temperature change rates with respect to load variation rates).

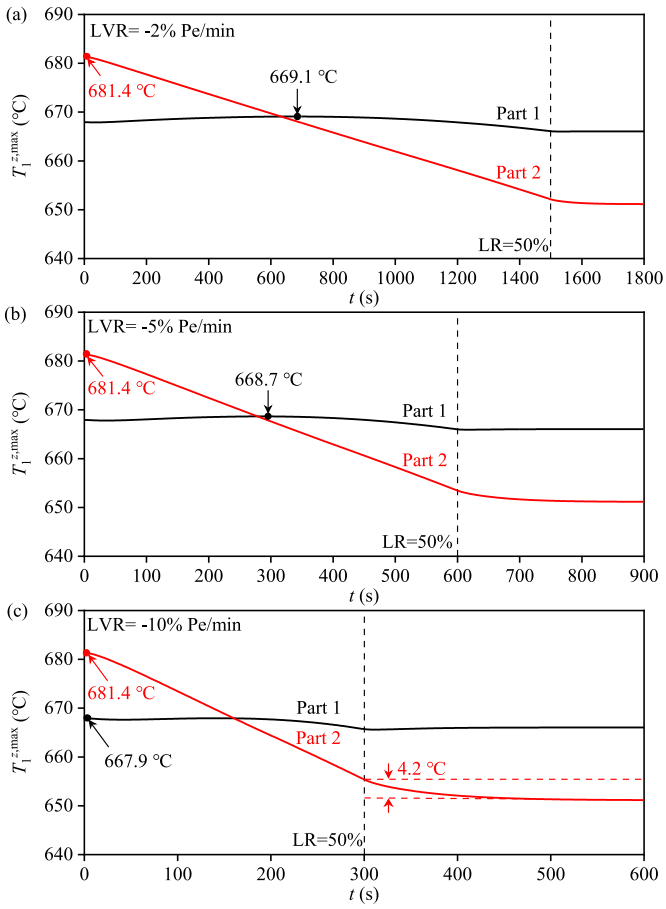


Fig. 15. Hot spot temperatures of cooling wall from 100 %THA to 50 %THA at load variation rates of (a) LVR = -2 % Pe/min, (b) LVR = -5 % Pe/min and (c) LVR = -10 % Pe/min.

Part 2, the hot spot temperatures show a decreasing trend during the load decrease process. After the load reaches 50 %, it continues to decline. At the LVR of −10 % Pe/min, it ultimately decreases by 4.2 °C. The maximum temperatures under different LVR are 681.4 °C, corresponding to the hot spot temperature at full load. Throughout the load decrease process, the temperatures also remain below the material temperature limit.

The hot spot locations z/L_{cw} during the load decrease process are shown in Fig. 16. In Part 1, the hot spot location gradually shifts downward, showing only a minor displacement. It decreases from z/L_{cw} = 0.20 at the beginning to z/L_{cw} = 0.16 at the end of the process. In Part 2, the hot spot location exhibits a rapid upward shift, rising from z/L_{cw} = 0.86 to z/L_{cw} = 1.0. The hot spot location at the beginning of load decrease process corresponds to that at the end of load increase process, and the reverse is also true. In addition, the location of the hot spot still remains unchanged in the circumferential direction, consistently located at the center of the fire-facing side of the tube. The influence of different LVR on hot spot location remains negligible during the load decrease process.

What is the temperature change rate of the pipe wall during load decrease process? The temperature change rates in both Part 1 and Part 2 exhibit monotonical decreasing trends versus time at $\eta_{q,c}$ = 1 (see Fig. 17a). In Part 1, the rates do not exceed −5 K/min at LVR = -2 % Pe/min and −5 % Pe/min. At LVR = -10 % Pe/min, it reaches −4.97 K/min at t = 5 min. Therefore, in Part 1, the temperature change rates remain within the safe range at all three LVRs. In Part 2, the rates remain within the criterion at LVR = -2 % Pe/min and −5 % Pe/min. However, at −10 % Pe/min, it reaches −5.03 K/min at t = 1min and continues to increase thereafter, which is not acceptable.

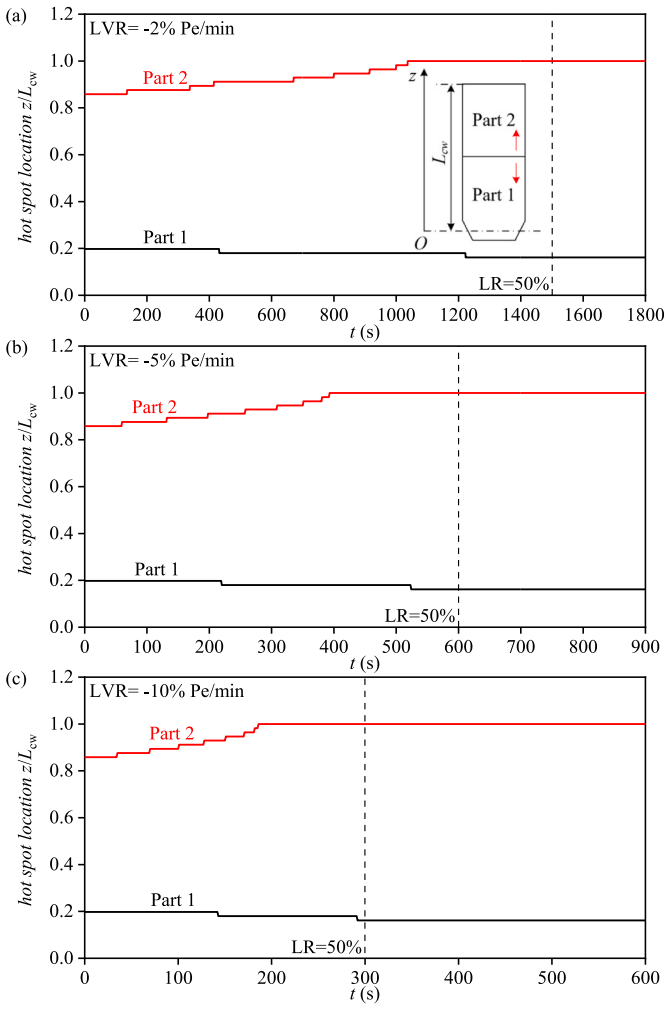


Fig. 16. Hot spot locations z/L_{cw} from 100 %THA to 50 %THA at load variation rates of (a) LVR = -2 % Pe/min, (b) LVR = -5 % Pe/min and (c) LVR = -10 % Pe/min.

Fig. 17b illustrates the relationship between max(dT/dt) and |LVR| under uniform heat flux distribution ($\eta_{q,c} = 1$) and non-uniform heat flux distributions ($\eta_{q,c} = 1.1$ and 0.9) over the furnace width. It is seen that max(dT/dt) quasi-linearly increases against |LVR|. The max(dT/dt)~ |LVR| curve with $\eta_{q,c} = 1$ is medially populated over the two sides of the curves with $\eta_{q,c} = 1.1$ and 0.9. Emphasizing the enhanced heating on the furnace width direction using $\eta_{q,c} = 1.1$ slightly decreases the critical load variation rate. Fig. 17b gives the critical LVR = -6.3 %Pe/min for load decrease condition, which is specified by Part 2.

It is noted that the above outcomes are achieved by imposing linear variations of parameters including flow rates, temperatures and pressures of CO_2 in the cycle side and heat flux in the furnace side (see Fig. 2). Alternatively, the deformed linear curve, called the piecewise variation mode, divides the whole variation cycle into several substages [31]. Practically, a parameter linearly increases to a level, maintains the level for a while, and linearly increases again, until the cycle ends. The piecewise mode can be regarded as the mode by introducing several perturbations on the linear curve. Here, the piecewise variation mode is performed for the flow rates of CO_2 and heat flux (see Fig. 18a–d). Effects of the piecewise mode on the transient variations of hot spot temperatures of the cooling walls for Part 1 and Part 2 are given in Fig. 18e–f. It is seen that the piecewise effect is weak compared with the linear variation mode. For Part 1, the maximum temperature is 671.2 °C, which is only 1.2 °C higher than that predicted with the linear variation mode. For Part 2, the temperature curve with the piecewise variation

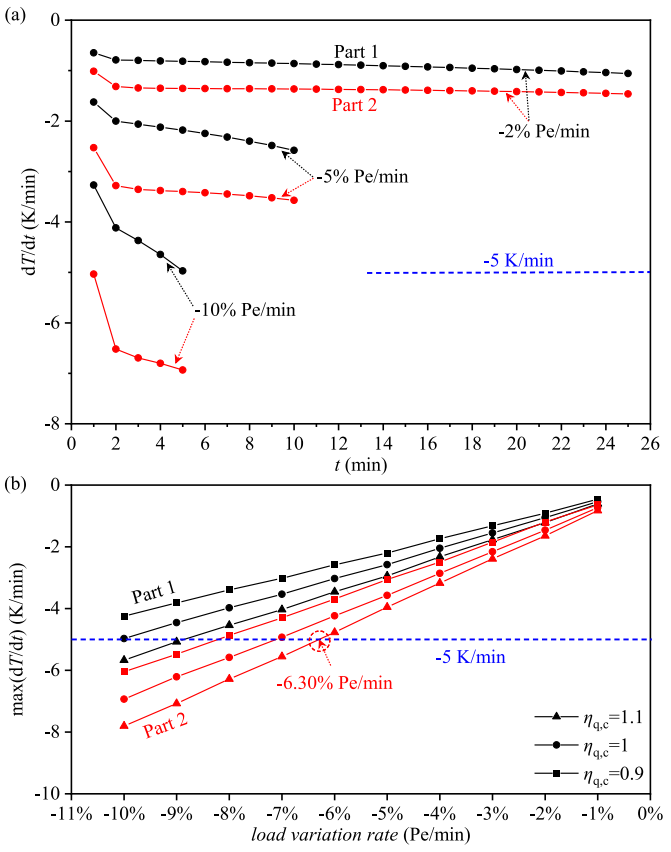


Fig. 17. Effect of load variation rates on temperature change rates of cooling wall for load decrease runs (a: temperature change rates versus time, b: quasi-linear distribution of maximum temperature change rates with respect to load variation rates).

mode slightly deviates from that with the linear variation mode. The maximum temperatures are identical to be 681.4 °C using both the linear and piecewise variation modes, because the maximum temperature takes place at the end of the variation cycle.

4.3. Comments on the transient characteristic of cooling walls

Based on the above analysis, the variation trends of hot spot temperatures under load increase and decrease conditions are not symmetric. Similar trends are also observed for temperature change rates of cooling walls. Furthermore, the critical LVR satisfying the 5 K/min limit are different for load increase and decrease conditions. These results indicate irreversible heat transfer processes for load increase and decrease runs, which could be attributed to the transient heat conduction of cooling walls. It should be noted that the initial conditions of the cooling walls at $t = 0$ are different for load increase and decrease runs. The non-symmetric phenomenon is related to the heat storage process of the cooling walls. The cooling walls absorb heat from the furnace to store energy during load increase stage. On the contrary, they release heat to CO_2 during load decrease stage.

It is noted that pressure drop type instability and density wave instability may occur in subcritical domain [56], affecting the system performance. The thermal system becomes more stable when increasing the system pressure [57]. The present paper deals with the supercritical CO_2 system. The critical parameters of CO_2 are 31.08 °C and 7.38 MPa for the critical temperature and pressure, respectively, which are significantly lower than those for the water-vapor media. This means that the critical temperature of CO_2 is reached at the room temperature level. For the sCO_2 boiler studied in this paper, the inlet temperature of CO_2 is in the 500 °C level. The CO_2 temperatures in the cooling walls

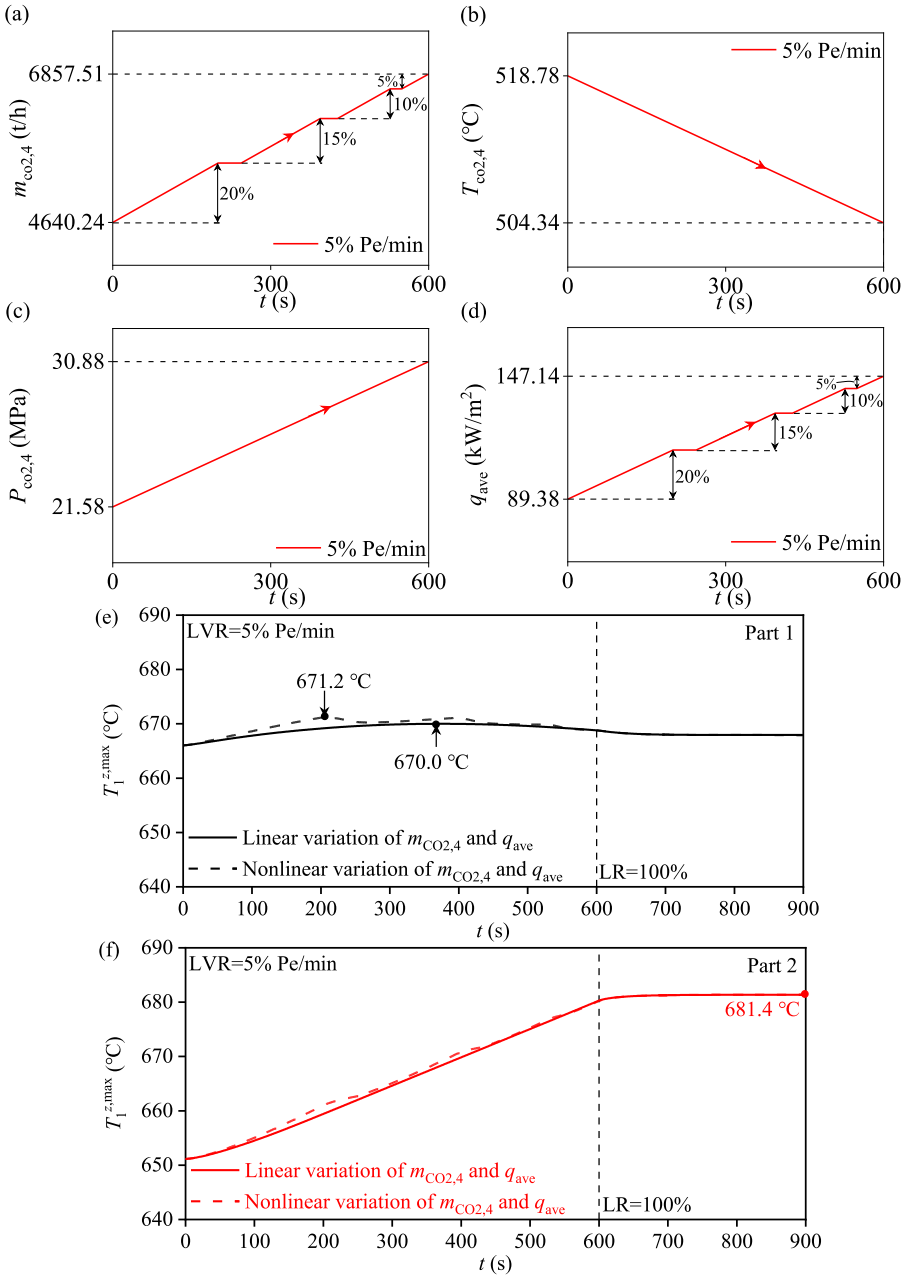


Fig. 18. Sensitivity analysis of the cooling wall performance under varying boundary conditions.

vary in a range of (500–600) °C, which are far beyond the pseudo-critical temperatures of (70–90) °C corresponding to the pressure range of (20–30) MPa, during load increase and decrease stages. The pseudo-critical temperature is never reached. In other words, there is no possibility of switching the supercritical flow to the subcritical two-phase flow during the load variation process. Hence, the phase changes related flow instabilities do not need to be considered here.

The present work and future perspective work are commented here. We emphasize that the coal-fired sCO_2 power generation system is a very complicated system, involving multi-spatial-temporal scales. Numerical simulation over the full time and space scales needs ultra-large computational resources. There are two types of numerical simulations, one focusing on the system level and the other focusing on the component level. In order to ensure the simulation process performed with acceptable computational resources, some simplifications are necessary. For the system level computation, numerical simulations yield dynamic variations of various parameters such as pressures, flow rates, thermal loads, and rotating speeds of compressors and turbines [58–60]. Because a set of components are coupled with each other in time series, one-dimensional model or lumped parameter method are used to deal with components [61]. Alternatively, for the computation of components, two or three dimensional models are used for the interest component, but simplifications should be made for other components except the interest one [62]. From the technical point of view, it is impractical to combine everything together or consider all the factors in one level's numerical simulation. The system complexity can be treated by the decoupling approach.

The present paper aims to provide dynamic analysis of the sCO_2 boiler, which is investigated in the component level instead of the system level. We note that in the Introduction section, various sCO_2 power generation technologies are being developed [7–9]. The key difference between the coal-fired power plant and other sCO_2 systems driven by solar energy and nuclear energy is the sCO_2 boiler. Because the sCO_2 boiler operates in the highest temperature region over the whole system,

dynamic analysis of the sCO_2 boiler is important to ensure its safe operation, especially during load variation stages. This is the reason why we focus on the hot spot temperatures and temperature change rates of the cooling walls of the sCO_2 boiler. We believe that numerical simulations coupling the two-dimensional cooling walls with the one-dimensional fluid flow in tubes are sufficient to give reasonable outcomes, by imposing heat flux in the furnace width and height directions. Dynamic characteristics of coal milling process, as well as compressors and turbines are not included in the present paper, but should be investigated in the future.

5. Conclusion

This study investigates the transient wall temperature of a cooling wall tube in a 300 MW sCO_2 boiler under system load changes ranging from 50 %THA to 100 %THA at different LVRs. The analysis focuses on hot spot temperature, hot spot location, and the temperature change rate of the tube wall during load variation. The effects of different LVRs are also analyzed. Key conclusions are summarized as follows:

(1) In Part 1, a downward flow configuration is adopted. Hot spot temperatures show only minor fluctuations during both load increase and decrease processes. Maximum temperatures increase with increase of LVR.
(2) In Part 2, an upward flow configuration is employed. Hot spot temperatures increase monotonically during load increase process, and decrease monotonically during load decrease process. Maximum temperatures remain unaffected by variations in LVR.
(3) Hot spot temperatures of cooling walls are below the material temperature limit for both load increase and decrease runs.
(4) Hot spot consistently appears at the center of fire-facing side of the tube and only shifts vertically along the height of the cooling wall. LVR has no significant influence on hot spot location.
(5) Critical load variation rates exist to be 6.21 % Pe/min and −6.30 % Pe/min for load increase and decrease cases, respectively, when the circumferential non-uniformity of furnace heat flux is considered.
(6) Load increase and decrease processes at same |LVR| are not thermally reversible and must be analyzed independently.

CRediT authorship contribution statement

Binghan Ma: Writing – original draft, Software, Methodology, Investigation, Formal analysis. **Jinliang Xu:** Writing – review & editing, Methodology, Funding acquisition, Conceptualization. **Haonan Zheng:** Validation, Supervision, Methodology. **Tianze Wang:** Writing – review & editing, Supervision, Methodology. **Jian Xie:** Writing – review & editing, Methodology.

Declaration of competing interest

We state that the manuscript titled as " Transient cooling wall temperatures of supercritical carbon dioxide boiler during load variation process " by Binghan Ma, Jinliang Xu, Haonan Zheng, Tianze Wang, Jian Xie does not have any conflict of interest including any financial, personal or other relationships with other people or organizations within three years of beginning the submitted work that could inappropriately influence, or be perceived to influence, the present work.

Acknowledgements

This work was supported by the Natural Science Foundation of China (52130608, 52176153).

Data availability

Data will be made available on request.

References

[1] Xu J, Sun E, Li M, Liu H, Zhu B. Key issues and solution strategies for supercritical carbon dioxide coal fired power plant. Energy 2018;157:227–46. https://doi.org/10.1016/j.energy.2018.05.162.
[2] Sun E, Xu J, Hu H, Li M, Miao Z, Yang Y, et al. Overlap energy utilization reaches maximum efficiency for S-CO2 coal fired power plant: a new principle. Energy Convers Manag 2019;195:99–113. https://doi.org/10.1016/j.enconman.2019.05.009.
[3] Sun E, Xu J, Li M, Liu G, Zhu B. Connected-top-bottom-cycle to cascade utilize flue gas heat for supercritical carbon dioxide coal fired power plant. Energy Convers Manag 2018;172:138–54. https://doi.org/10.1016/j.enconman.2018.07.017.
[4] Jiang Y, Liese E, Zitney SE, Bhattacharyya D. Design and dynamic modeling of printed circuit heat exchangers for supercritical carbon dioxide Brayton power cycles. Appl Energy 2018;231:1019–32. https://doi.org/10.1016/j.apenergy.2018.09.193.
[5] Wang T, Xu J, Wang Z, Zheng H, Qi J, Liu G. Irreversible losses, characteristic sizes and efficiencies of sCO2 axial turbines dependent on power capacities. Energy 2023;275. https://doi.org/10.1016/j.energy.2023.127437.
[6] Wang T, Xu J, Zheng H, Qi J. Performance and sizes of sCO2 multistage axial compressors at various power capacities. J Therm Sci 2025;34:352–73. https://doi.org/10.1007/s11630-025-2091-8.
[7] Xu J, Liu C, Sun E, Xie J, Li M, Yang Y, et al. Perspective of S−CO2 power cycles. Energy 2019;186. https://doi.org/10.1016/j.energy.2019.07.161.
[8] Wang X, Wang R, Bian X, Cai J, Tian H, Shu G, et al. Review of dynamic performance and control strategy of supercritical CO2 Brayton cycle. Energy and AI 2021;5. https://doi.org/10.1016/j.egyai.2021.100078.
[9] Guo JQ, Li MJ, He YL, Jiang T, Ma T, Xu JL, et al. A systematic review of supercritical carbon dioxide(S-CO2) power cycle for energy industries: technologies, key issues, and potential prospects. Energy Convers Manag 2022;258. https://doi.org/10.1016/j.enconman.2022.115437.
[10] Ma T, Li MJ, Xu JL, Ni JW, Tao WQ, Wang L. Study of dynamic response characteristics of S-CO2 cycle in coal-fired power plants based on real-time microgrid load and a novel synergistic control method with variable working conditions. Energy Convers Manag 2022;254. https://doi.org/10.1016/j.enconman.2022.115264.
[11] Deng T, Li X, Wang Q, Ma T. Dynamic modelling and transient characteristics of supercritical CO2 recompression Brayton cycle. Energy 2019;180:292–302. https://doi.org/10.1016/j.energy.2019.05.074.
[12] Liese E, Albright J, Zitney SA. Startup, shutdown, and load-following simulations of a 10 MWe supercritical CO2 recompression closed Brayton cycle. Appl Energy 2020;277. https://doi.org/10.1016/j.apenergy.2020.115628.
[13] Wang R, Wang X, Shu G, Tian H, Cai J, Bian X, et al. Comparison of different load-following control strategies of a sCO2 Brayton cycle under full load range. Energy 2022;246. https://doi.org/10.1016/j.energy.2022.123378.
[14] Wang X, Wang R, Bian X, Cai J, Tian H, Shu G, et al. Review of dynamic performance and control strategy of supercritical CO2 Brayton cycle. Energy and AI 2021;5. https://doi.org/10.1016/j.egyai.2021.100078.
[15] Ma T, Li MJ, Xue XD, Guo JQ, Wang WQ, Jiang T. Study of peak-load regulation characteristics of a 1000MWe S-CO2 coal-fired power plant and a comprehensive evaluation method for dynamic performance. Appl Therm Eng 2023;221. https://doi.org/10.1016/j.applthermaleng.2022.119892.
[16] Zhou J, Zhu M, Xu K, Su S, Tang Y, Hu S, et al. Key issues and innovative double-tangential circular boiler configurations for the 1000 MW coal-fired supercritical carbon dioxide power plant. Energy 2020;199. https://doi.org/10.1016/j.energy.2020.117474.
[17] Liu C, Xu J, Li M, Wang Z, Xu Z, Xie J. Scale law of sCO2 coal fired power plants regarding system performance dependent on power capacities. Energy Convers Manag 2020;226. https://doi.org/10.1016/j.enconman.2020.113505.
[18] Zhu B, Xu J, Wu X, Xie J, Li M. Supercritical “boiling” number, a new parameter to distinguish two regimes of carbon dioxide heat transfer in tubes. Int J Therm Sci 2019;136:254–66. https://doi.org/10.1016/j.ijthermalsci.2018.10.032.
[19] Liu C, Xu J, Li M, Wang Q, Liu G. The comprehensive solution to decrease cooling wall temperatures of sCO2 boiler for coal fired power plant. Energy 2022;252. https://doi.org/10.1016/j.energy.2022.124021.
[20] Kim S, Choi S. Dynamic simulation of the water-steam flow in a supercritical once-through boiler. J Mech Sci Technol 2017;31:4965–75. https://doi.org/10.1007/s12206-017-0945-z.
[21] Wang C, Chen X, Liu B, Liu K, Han Y, Wang L, et al. Dynamic analysis for ultra-supercritical boiler water wall considering uneven heat flux distribution and combustion instability. Int J Heat Mass Tran 2025;236. https://doi.org/10.1016/j.ijheatmasstransfer.2024.126269.
[22] Wang D, Zhao Y, Gao W, Chen W, Wang C, Yan J. Revised control strategy for coal-fired power plants during transient processes considering heat transfer deterioration of cooling wall: flexibility enhancement and security operation. Int J Heat Mass Tran 2025;251. https://doi.org/10.1016/j.ijheatmasstransfer.2025.127372.
[23] Liu K, Wang L, Bai W, Che D. Comparative study on dynamic characteristics of 600 MW supercritical coal-fired boilers using CO2 and water as working fluids. Energy 2025;314. https://doi.org/10.1016/j.energy.2024.134296.

[24] Zheng H, Miao Z, Xu J. Partial load operation characteristics of supercritical CO2 coal-fired power generation system. Energy 2024;291. https://doi.org/10.1016/j.energy.2024.130415.
[25] Li H, Zhang Y, Bai W, Yang Y, Li K, Gao W, et al. Control strategies and dynamic experimental tests on the wide-range and rapid load regulation of a first pilot multi-megawatts fossil-fired supercritical CO2 power system. Energy Convers Manag 2023;279. https://doi.org/10.1016/j.enconman.2023.116748.
[26] Kruthika U, Paneerselvam S. Enhanced set-point tracking in a Boiler Turbine System via decoupled MIMO linearization and comparative LQR-based control strategy. Results Eng 2025;25. https://doi.org/10.1016/j.rineng.2025.103914.
[27] Hu X, Wang T, Wu H, Zhou T, Zhang M, Song Q, et al. Research on thermal inertia in CFB boilers: mechanisms, effects, and a novel retrofit approach. Appl Therm Eng 2025;274. https://doi.org/10.1016/j.applthermaleng.2025.126693.
[28] Jin B, Yao W, Liu K, Lu S, Luo X, Liang Z. Self-optimizing control and safety assessment to achieve economic and safe operation for oxy-fuel combustion boiler island systems. Appl Energy 2022;323. https://doi.org/10.1016/j.apenergy.2022.119397.
[29] Jiang M, Fan H, Kang D, Shi Z, Wang W, Qu D, et al. Thermal inertia and stress of steam separator during variable load process based on fluid-structure-heat coupling. Energy 2025;322. https://doi.org/10.1016/j.energy.2025.135654.
[30] Hedrick K, Hedrick E, Omell B, Zitney SE, Bhattacharyya D. Dynamic modeling, parameter estimation, and data reconciliation of a supercritical pulverized coal-fired boiler. Ind Eng Chem Res 2022;61:16764–79. https://doi.org/10.1021/acs.iecr.2c01977.
[31] Liu K, Wang C, Wang L, Liu B, Ye M, Guo Y, et al. Dynamic performance analysis and control strategy optimization for supercritical coal-fired boiler: a dynamic simulation. Energy 2023;282. https://doi.org/10.1016/j.energy.2023.128712.
[32] Lü JF. Investigation on heat flux and hydrodynamics of water wall of a supercritical pressure circulating fluidized bed boiler. Tsinghua University; 2004.
[33] Brown GO. ENVIRONMENTAL AND WATER RESOURCES HISTORY the history of the darcy-weisbach equation for pipe flow resistance. n.d.
[34] Wang Z, Sun B, Wang J, Hou L. Experimental study on the friction coefficient of supercritical carbon dioxide in pipes. Int J Greenh Gas Control 2014;25:151–61. https://doi.org/10.1016/j.ijggc.2014.04.014.
[35] Seamless stainless steel tubes for boiler and heat exchanger. National standards of P.R.C, GB; 2013.
[36] Zima W, Nowak-Ocłoń M, Ocłoń P. Novel online simulation-ready models of conjugate heat transfer in combustion chamber waterwall tubes of supercritical power boilers. Energy 2018;148:809–23. https://doi.org/10.1016/j.energy.2018.01.178.
[37] Zima W. Analysis of temperature drops on the wall thickness of a supercritical boiler water-wall tube. Therm Sci 2019;23:1091–100. https://doi.org/10.2298/TSCI19S4091Z.
[38] Kline N, Feuerstein F, Tavoularis S. Onset of heat transfer deterioration in vertical pipe flows of CO2 at supercritical pressures. Int J Heat Mass Tran 2018;118:1056–68. https://doi.org/10.1016/j.ijheatmasstransfer.2017.11.039.
[39] Zhang Q, Li H, Kong X, Liu J, Lei X. Special heat transfer characteristics of supercritical CO2 flowing in a vertically-upward tube with low mass flux. Int J Heat Mass Tran 2018;122:469–82. https://doi.org/10.1016/j.ijheatmasstransfer.2018.01.112.
[40] Yang S, Tao W. In: Heat transfer. fourth ed. Beijing, China: Higher Education Press; 2006.
[41] Li F, Bai B. A model of heat transfer coefficient for supercritical water considering the effect of heat transfer deterioration. Int J Heat Mass Tran 2019;133:316–29. https://doi.org/10.1016/j.ijheatmasstransfer.2018.12.121.
[42] Lei X, Guo Y, Zhang W, Li H, Li L. Development of heat transfer correlation for supercritical water in vertical upward tubes. Heat Transf Eng 2019;40:652–66.
[43] Zhu B, Xu J, Yan C, Xie J. The general supercritical heat transfer correlation for vertical up-flow tubes: k number correlation. Int J Heat Mass Tran 2020;148. https://doi.org/10.1016/j.ijheatmasstransfer.2019.119080.
[44] Bishop AA, Sandberg RO, Tong L. Forced convection heat transfer to water at near-critical temperatures and super-critical pressures. 1964. Pittsburgh, PA, USA.
[45] Jackson JD. Fluid flow and convective heat transfer to fluids at supercritical pressure. Nucl Eng Des 2013;264:24–40. https://doi.org/10.1016/j.nucengdes.2012.09.040.
[46] Jackson JD, Hall WB. Influences of buoyancy on heat transfer to fluids flowing in vertical tubes under turbulent conditions. Turbulent Forced Convection in Channels and Bundles 1979:613–40.
[47] Yu J, Jia B, Wu D, Wang D. Optimization of heat transfer coefficient correlation at supercritical pressure using genetic algorithms. Heat and Mass Transfer/Waerme-Und Stoffuebertragung 2009;45:757–66. https://doi.org/10.1007/s00231-008-0475-4.
[48] Gupta S, Saltanov E, Mokry SJ, Pioro I, Trevani L, McGillivray D. Developing empirical heat-transfer correlations for supercritical CO2 flowing in vertical bare tubes. Nucl Eng Des 2013;261:116–31. https://doi.org/10.1016/j.nucengdes.2013.02.048.
[49] Alshahrani AM, Lim CH, Kim J, Zhang Y. Transient thermal stresses developed during speed sintering of 3 mol% yttria-stabilized tetragonal zirconia polycrystals. Dent Mater 2023;39:522–8. https://doi.org/10.1016/j.dental.2023.04.004.
[50] Wang R, Tian H, Wang X, Tian R, Wu Z. Analysis of wall temperature change rate limiting supercritical CO2 power system flexibility. Energy 2025;316. https://doi.org/10.1016/j.energy.2025.134448.
[51] Park SY, On SY, Kim J, Lee J, Kim TS, Wardle BL, et al. Electronic packaging enhancement engineered by reducing the bonding temperature via modified cure cycles. ACS Appl Mater Interfaces 2023;15:11024–32. https://doi.org/10.1021/acsami.2c21229.
[52] Underwood C, Lamb D, Irvine S, Mardhani S, Lassakeur A. IAC-22-C3.3.8 six years of spaceflight results from the AlSat-1N Thin-Film Solar Cell (TFSC) experiment. Acta Astronaut 2023;213:20–8. https://doi.org/10.1016/j.actaastro.2023.08.034.
[53] Taler J, Dzierwa P, Taler D, Harchut P. Optimization of the boiler start-up taking into account thermal stresses. Energy 2015;92:160–70. https://doi.org/10.1016/j.energy.2015.03.095.
[54] Li X, Qin Z, Dong K, Wang L, Lin Z. Experimental study of the startup of a supercritical CO2 recompression power system. Energy 2023;284. https://doi.org/10.1016/j.energy.2023.128538.
[55] Liu K, Guo Y, Wang L, Fan G, Che D. Control of supercritical CO2 Brayton cycle for fast and efficient load variation processes. Appl Therm Eng 2024;244. https://doi.org/10.1016/j.applthermaleng.2024.122797.
[56] O'Neill LE, Mudawar I. Review of two-phase flow instabilities in macro- and micro-channel systems. Int J Heat Mass Tran 2020;157. https://doi.org/10.1016/j.ijheatmasstransfer.2020.119738.
[57] Wanstall CT, Ferraiuolo G, Román A. On the analysis of static thermal instabilities occurring in two-phase flow systems. Int J Multiphas Flow 2024;180. https://doi.org/10.1016/j.ijmultiphaseflow.2024.104975.
[58] Wang R, Li X, Qin Z, Cai J, Bian X, Wang X, et al. Control strategy for actual constraints during the start–stop process of a supercritical CO2 Brayton cycle. Appl Therm Eng 2023;226. https://doi.org/10.1016/j.applthermaleng.2023.120289.
[59] Ma T, Li MJ, Xu JL, Ni JW, Tao WQ, Wang L. Study of dynamic response characteristics of S-CO2 cycle in coal-fired power plants based on real-time micro-grid load and a novel synergistic control method with variable working conditions. Energy Convers Manag 2022;254. https://doi.org/10.1016/j.enconman.2022.115264.
[60] Liese E, Albright J, Zitney SA. Startup, shutdown, and load-following simulations of a 10 MWe supercritical CO2 recompression closed Brayton cycle. Appl Energy 2020;277. https://doi.org/10.1016/j.apenergy.2020.115628.
[61] Zhao Q, Xu J, Hou M, Chong D, Wang J, Chen W. Dynamic characteristic analysis of SCO2 Brayton cycle under different turbine back pressure modes. Energy 2024;293. https://doi.org/10.1016/j.energy.2024.130563.
[62] Yang Y, Li H, Zhang Y, Bai W, Yao M. Coupled modeling of combustion and heat transfer process of a supercritical CO2 boiler. Fuel 2020;279. https://doi.org/10.1016/j.fuel.2020.118294.

Nomenclature

A: cross-sectional area, m^2
c: specific heat capacity, kJ/(kg·K)
d: diameter, mm
f: friction coefficient
g: gravity acceleration, m/s^2
G: mass flux, $kg/(m^2 \cdot s)$
i: enthalpy, kJ/kg
k: thermal conductivity, W/(m·K)
K: non-dimensional parameter representing evaporation induced momentum force relative to inertia force
L: length, m
m: mass flow rate, t/h
n: number of tubes in a heat exchanger module
Nu: Nusselt number
P: pressure, MPa
P_f: friction pressure drop, MPa
Pr: Prandtl number
q: heat flux, kW/m^2
r: radius, mm
Re: Reynolds number
s: tube pitch, mm
t: time, s
T: temperature, °C
u: velocity, m/s
U: circumference, m
w_x *or* w_y: width or depth of furnace, m
z: coordinate along furnace height, m

Greek symbols

α: heat transfer coefficient, $W/(m^2 \bullet K)$
β: inclination angle of waterwall tube
δ_w: thickness of fin, mm
Δ: absolute roughness of cooling wall, mm
Δr: thickness of tube, mm
Δx: spatial step in x directions, mm
$\Delta\widehat{\varphi}$: radians between control volumes, rad
$\eta_{q,c}$: non-uniformity coefficient of heat flux along furnace circumference
$\eta_{q,h}$: non-uniformity coefficient of heat flux along furnace height
ρ: density, kg/m^3
ϕ: angle coefficient
τ: time, s
μ: dynamic viscosity, Pa·s

Subscripts

ave: average
b: boiler
cw: cooling wall
f: fluid
in: inner
max: maximum
mi: middle
out: outer
w: wall
wi: inner wall

Abbrevations

ACM: Aspen Custom Modeler
BFD1: first-order backward finite difference
C: compressor
EAP: external air preheater
HRH: high temperature reheater in boiler
HTR: high temperature recuperator
LR: load ratio
LRH: low temperature reheater in boiler
LTR: low temperature recuperator
LVR: load variation rate
RC: recompression cycle
RH: reheating
SH: superheater in upper furnace
T: turbine
THA: turbine heat acceptance
V: valve